**The Texaco/UOP HF Alkylation Additive Technology: Aerosolization Reduction Effects** [1]

G. A. Melhem, ioMosaic Corporation, Salem, New Hampshire
K. R. Comey, Texaco Inc., Port Arthur, Texas
R. M. Gustafson, Texaco Inc., Houston, Texas

# Summary

This paper examines typical release conditions leading to aerosol formation in existing HF alkylation technology. The variables affecting aerosol formation in the mechanical and thermal breakup regimes are identified. The properties of these key variables are altered chemically using an additive to reduce aerosol formation for the entire operation envelop without degradation of alkylation efficiency.

Small and large scale tests were conducted to experimentally verify the benefits of the additive in both the mechanical and thermal breakup regimes. This paper summarizes the findings of these experiments and presents a detailed method for estimating the release, droplet formation and dynamics and dispersion behavior of chemically reacting systems. This method is validated using the small and large scale data and is used to perform sensitivity analysis to assess the impact of storage temperature, pressure, composition, atomospheric and site conditions on aerosol and toxic hazard zone reduction.

# Background

Anhydrous hydrofluoric acid (AHF) is used in the petroleum industry as a catalyst for the production of high octane gasoline by the isobutane-isobutylene alkylation reaction. The alkylate product is a key blending component in the production of reformulated gasoline which will meet new federal fuel specifications since it contains virtually no aromatic or olefinic components. Episodic releases of pressurized, superheated anhydrous hydrofluoric acid predominantly produce an aerosol. The aerosol cloud formed may contain concentrations above acceptable exposure criteria [1]. Episodic releases at several refineries have resulted in increasing political pressure to replace existing hydrofluoric acid (HF) alkylation units with sulfuric acid alkylation units. The estimated cost of converting a single HF alkylation unit to sulfuric acid ranges from 50 to more than 100 million dollars, depending upon the unit capacity.

[1] This paper appeared in the proceedings of the International Conference and Workshop On Modeling and Mitigating The Consequences of Accidental Releases of Hazardous Materials, AIChE/CCPS, September 26-29, 1995.

# Aerosol Formation

The potential hazard of a liquid toxic or flammable substance when released to the atmosphere is a strong function of source characteristics such as geometry, temperature, density, composition, aerosol fraction, and release rate. Reducing the source emission rate and duration is key to reducing exposure concentrations and durations below established safe threshold values.

Stored liquids which remain in the liquid state after release usually present less hazard because of possible post-release mitigation action. Materials that become airborne immediately upon release, such as HF, chlorine, ammonia, are very difficult to mitigate, especially when large quantities are discharged over short periods of time.

Major factors that influence the amount of a given material which will become airborne upon release to the atmosphere include the material's vapor pressure and normal boiling point. These properties usually determine whether during discharge a material will be vapor, liquid, or a flashing liquid. The amount of superheated liquid that is converted to vapor upon release, or the flash fraction, can be calculated using thermodynamics. However, this flash fraction does not account for the aerosolized liquid fraction carried with the vapor when sufficient energy is available in the superheated liquid to cause liquid breakup.

The aerosolization process is important. Liquid aerosols increase the airborne vapor cloud mass and density which causes the cloud to become heavier than air. Cloud density is also increased when entrained water vapor condenses. The heavier vapor cloud produced by aerosolization of liquid can result in significantly larger impact areas. The liquid that rains out forms an evaporating pool whose contribution to the source strength can be significant if the released material has a low normal boiling point.

## Mechanical Breakup

Mechanical breakup forms aerosols by producing flows at speeds which result in surface stresses that cause liquid droplets of a given diameter to become unstable and breakup into smaller droplets. The maximum stable drop diameter can be related to the Weber number, $N_{We}$:

$$N_{We} = \frac{\rho_s u^2 d_d}{\sigma_d} \tag{1}$$

where, $u$, is the velocity of the liquid jet relative to surrounding medium. Experiments indicate that a critical Weber number value of 10 to 20 is sufficient to cause aerosolization for small orifice diameters (see Brown and York [2], Bushnell and Gooderum [3], Hinze [4]).

The critical Weber number value depends on the flow pattern. The critical Weber number necessary to cause droplet breakup in an air stream is different from that required for breakup of a droplet in viscous flow or emulsifications in turbulent flow. The critical Weber number also depends on droplet viscosity:

$$N_{We_c} = C\left[1 + f(N_{Vi})\right] \tag{2}$$

Figure 1: Dependence of maximum stable droplet diameter on 1/2 $u^2$ for a Weber number of 12

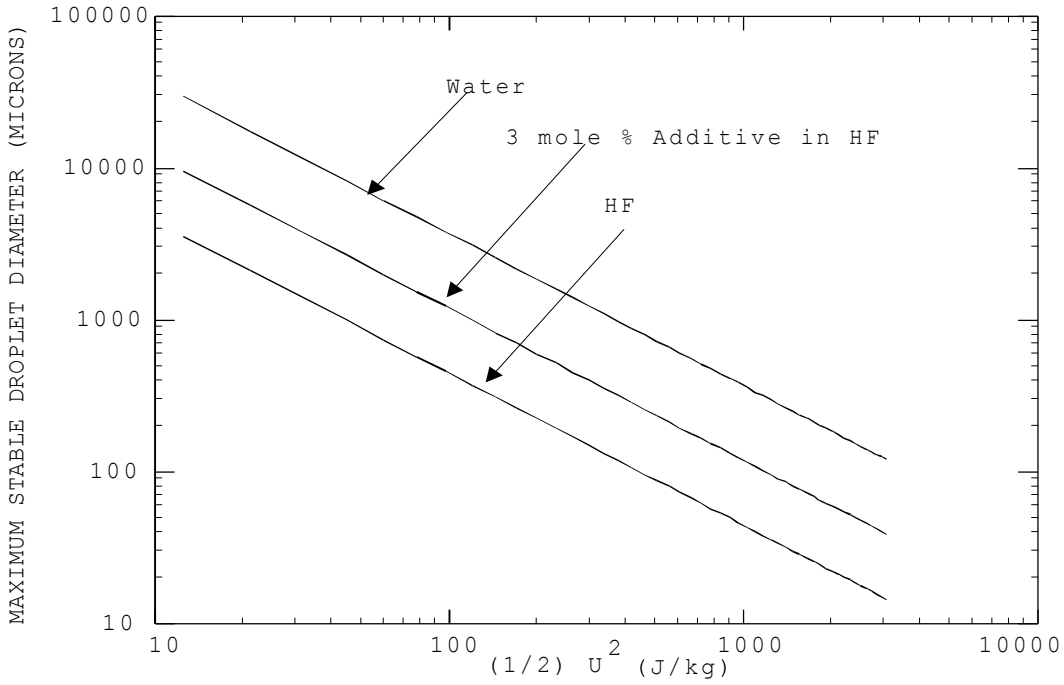


where $C$ is the critical Weber number at $N_{Vi} = 0$ and $N_{Vi}$ is a viscosity group number given by:

$$N_{Vi} = \frac{\mu_{l,d}}{\sqrt{\rho_{l,d}\sigma_d d_d}} \tag{3}$$

At values of $N_{Vi} > 0.5$, the relative velocity difference between the liquid droplet and ambient air decreases markedly during breakup. Brodkey [5] provides an empirical equation which illustrates the effect of the viscosity number on the critical Weber number:

$$N_{We_c} = 14N_{Vi}^{1.6} + [N_{We_c}]_{N_{Vi}=0} \tag{4}$$

At small viscosity numbers, the maximum stable droplet diameter is directly proportional to the fluid surface tension. Higher surface tension will lead to the formation of larger droplets. Figure 1 illustrates the dependence of maximum stable droplet diameter on $1/2u^2$, where $u$ is the difference between release velocity and that of the surroundings.

## Thermal Breakup

Thermal breakup is encountered in releases of superheated liquids and is caused by the flashing of liquid to vapor and the subsequent bubble growth as well as the relative velocity between the vapor and liquid. As the vapor bubble grows, it extends the surrounding liquid into a thin film. When the bubble ruptures, the liquid film breaks up into many small droplets.

Figure 2: Pressure and surface tension forces acting on a spherical bubble

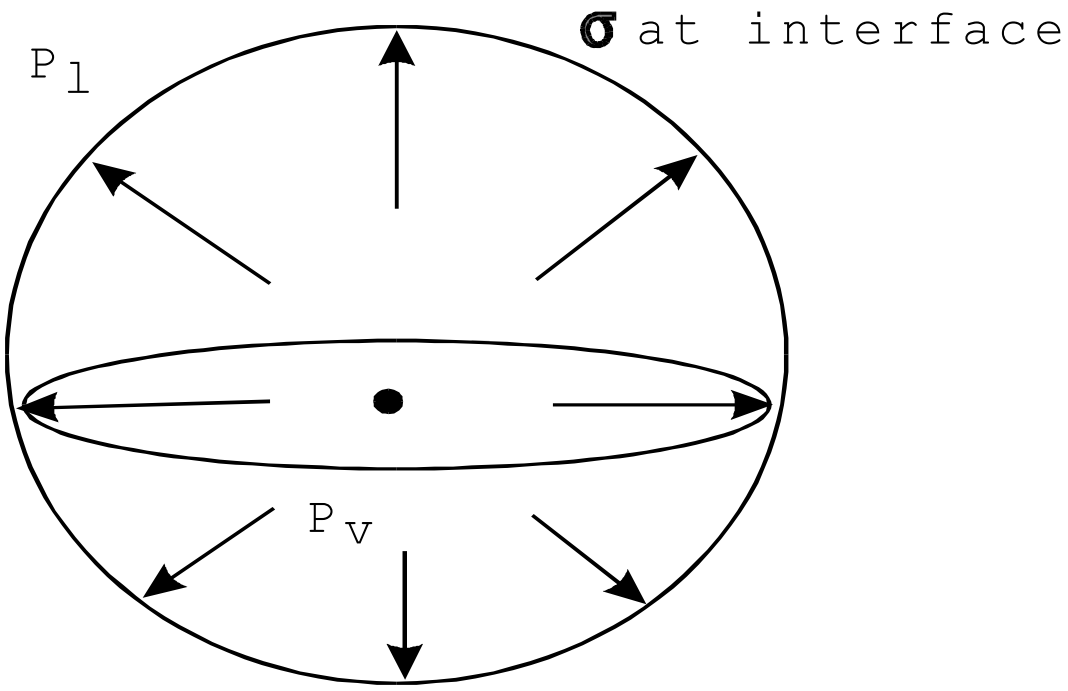


Let us examine the pressure and surface tension forces acting on a spherical bubble such as the one shown in Figure 2. Inside the bubble, the vapor is at $P_v$ and the outside liquid is at $P_l$ where $(P_v > P_l)$. For the pressure force to be balanced by surface tension forces, the following equality must be satified:

$$(P_v - P_l)\pi r_1^2 = 2\pi r_1 \sigma \tag{5}$$

If the vapor bubble is saturated at $P_v$ then $T_v$ is greater than $T_l$. Heat is transferred from the vapor to the liquid and the bubble will collapse due to condensation. In order for the bubble to grow, heat must be transferred from the liquid to the vapor, i.e. $T_l > T_v$ or the liquid must be superheated.

For a spherical vapor bubble in equilibrium with the surrounding liquid, pressure is balanced by surface tension:

$$P_v - P_l = \frac{2\sigma}{r_1} \tag{6}$$

For bubble growth to take place $P_v - P_l$ must be positive. For evaporation to take place $T_l - T_v$ must be positive. If we approximate the vapor pressure slope using the Clapeyron equation, integrate and combine the result with Equation 6 we find:

$$T_v - T_{sat} = \frac{R_g T_{sat} T_v}{\underline{\lambda}} \ln\left[1 + \frac{2\sigma}{P_l r_1}\right] \tag{7}$$

Figure 3: Dependence of maximum stable droplet diameter on available energy for a modified Weber number of 500

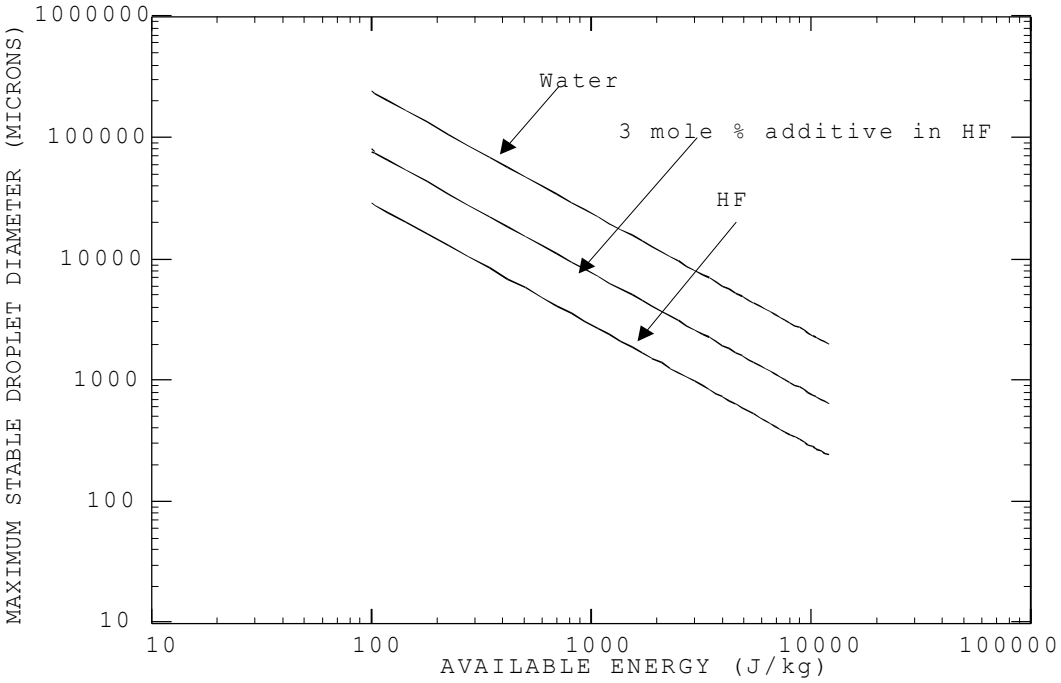


Assuming that $T_v - T_l$ is small at elevated pressure, the above equation simplifies to:

$$T_v - T_{sat} \cong \frac{2R_g T_{sat}^2 \sigma}{\lambda P_l r_1} = \Delta T_c \tag{8}$$

For a fixed value of $\Delta T_c$, nuclei of radius $r_1$ or larger will grow and become bubbles. Nuclei with smaller radius will collapse. As a bubble begins to grow, surface tension forces become negligible. This results in a steady increase in the rate of bubble growth and evaporation at the bubble surface. The heat of vaporization is supplied by heat flow from the bulk of the liquid which is at a lower temperature to the bubble boundary.

The degree of superheat must be greater or equal to a critical value necessary for bubble nucleation (see Ianello et al. [6]):

$$\Delta T_{\mathrm{C}} = \frac{2R_g T_{sat}^2 \sigma}{\lambda P_s r_{\mathrm{site}}} \tag{9}$$

where $r_{\mathrm{site}}$ is the radius of nucleation sites present in the fluid. Values of $r_{\mathrm{site}}$ range from $10^{-6}$ to $10^{-11}$ m. The critical superheat typically ranges from 5 to 15 K for many fluids of interest. Nucleation of bubbles can also be attributed to surface imperfections such as cavities and the presence of gas nuclei.

The mathematical treatment of bubble growth is complex. Forester and Zuber [7] assumed that the dominating heat transfer mechanism is conduction. Zwick and Plasset [8] assumed a single

heat transfer resistance provided by a thin liquid shell surrounding the bubble. Neglecting gravity effects, they derive the following partial differential equation to relate pressure and bubble radius as a function of time for a spherical bubble:

$$r\frac{\partial^2 r}{\partial t^2} + \frac{3}{2}\left(\frac{\partial r}{\partial t}\right)^2 + \frac{2\sigma}{r_1\rho_l} = \frac{P_v - P_l}{\rho_l} \tag{10}$$

The results of Zuber and Forester [7] and Zwick and Plasset [8] are in good agreement. The solution of equation 10 was simplified by considering a sequence of four bubble regimes (also see Brown and York [2]; Shepherd and Strutevart [9]; Kwak and Lee [10]):

1. A surface-tension controlled stage where the bubble grows from a critical radius, i.e., nucleation. The smallest bubble capable of growth has a radius of:

$$r_1 = \frac{2\sigma_d}{P_{sat} - P_s} \tag{11}$$

2. An inertia-controlled stage where the bubble grows at a constant rate determined by the vapor pressure and the density of the superheated liquid. This process happens very fast (on the order of microseconds) and the final bubble radius is about 10 times $r_1$:

$$r_2 = 10r_1 \tag{12}$$

3. An asymptotic stage where bubble growth is limited by heat transfer and follows a linear dependence on the square root of time:

$$r_3 = r_2 + \left[F\left(\frac{\rho_f}{\rho_0}\right)(\pi\alpha)^{1/2}\right]t^{1/2} \tag{13}$$

   where, $F$ is the flash fraction and $\alpha$ is the thermal diffusivity. The ratio of densities is a measure of the change in volume due to flashing. The last term is a measure of the rate of heat conduction from the liquid to the vapor. The factor multiplying the square root of time is referred to as the bubble growth rate and has the unit of $\mathrm{m/s^{1/2}}$.

4. After the bubble has grown large enough (1 mm in diameter), its buoyancy becomes significant and it will rise through the liquid. Bubble rise is opposed by frictional drag on the bubble surface.

The presence of inert gas as molecules dispersed through the liquid or as colloidal suspension of sub-microscopic gas bubbles will reduce the critical nucleation superheat. If the inert gas has a partial pressure of $p_g$ where:

$$p_g = \frac{N_g R_g T_v}{\frac{4}{3}\pi r^3} \tag{14}$$

The gas-vapor bubble equilibrium relation given by equation 6 is re-written to account for the inert gas partial pressure:

$$P_v - P_l = \frac{2\sigma}{r_1} - p_g \tag{15}$$

It can be shown that the critical nucleation superheat is approximately equal to:

$$T_v - T_{sat} \cong \frac{2R_g T_{sat}^2}{\underline{\lambda} r P_{sat}} \left[ \sigma - \frac{3N_g R_g T_v}{8\pi r^2} \right] \tag{16}$$

The maximum stable radius of a gas-vapor bubble containing $N_g$ kmol of gas is found by setting $\frac{\partial}{\partial r}(P_v - P_l)$ to zero:

$$r_{g,c} = 3\sqrt{\frac{N_g R_g T_v}{8\pi\sigma}} \tag{17}$$

The critical excess pressure is given by:

$$(P_v - P_l)_c = \frac{4}{9}\sigma\sqrt{\frac{8\pi\sigma}{N_g R_g T_v}} \tag{18}$$

The critical radius can be expressed as a function of the excess pressure:

$$r_{g,c} = \frac{4\sigma}{3(P_v - P_l)} \tag{19}$$

A gas-vapor nucleus greater than $r_{g,c}$ will continue to grow. As the liquid temperature increases, the vapor pressure increases resulting in a larger pressure difference $(P_v - P_l)$ and smaller gas nuclei become active at the higher pressure difference.

At small orifice diameters thermal breakup is mainly dominated by surface stresses due to relative velocity effects. The transition to full atomization is instantaneous and depends on a critical superheat value which yields a critical relative velocity value. At large orifice diameters, the velocity effect diminishes and the flashing mechanism leading to bubble growth becomes important.

Lienhard and Day [11] suggest that liquid jet breakup will occur by flashing (thermal) if the flashing breakup length is smaller than the mechanical breakup length and if radial heat transfer in the jet is not rapid enough to prevent flashing in the jet interior such that vaporization will only take place at the surface. They define the following lengths for mechanical breakup:

**Capillary Breakup**

$$l_b = 11.5 d_j \sqrt{N_{We_j}} \text{ for } N_{Re_j} < 48000 \tag{20}$$

**Aerodynamic Breakup**

$$l_b = 2.75 \times 10^{10} d_j \sqrt{\frac{N_{We_j}}{N_{Re_j}^2}} \text{ for } N_{Re_j} > 48000 \tag{21}$$

The length for **thermal breakup** (flashing) is defined as the product of the jet velocity $u_j$ and the dwell time required for bubble nucleation and growth:

$$l_b = u_j \left[ 2.21 \times 10^{13} \left( \frac{\sigma^3 \sqrt{\rho_l}}{d_j^2 (P_{j,l} - P_s)^{7/2}} \right) + \left( \frac{d_j^2}{\pi \alpha} \right) \left( \frac{\rho_v}{\rho_l} \right)^2 \left( \frac{\lambda}{C p_l (T_{j,l} - T_{sat})} \right)^2 \right] \tag{22}$$

where $T_{sat}$ is the bubble point at ambient pressure and $T_{j,l}$ is the superheated liquid jet temperature and $P_{j,l}$ is the vapor pressure of the liquid at the jet temperature. The jet will not breakup by flashing if the following condition is satisfied:

$$2.12 \times 10^{13} \frac{\sigma}{d_j (P_{j,l} - P_{sat})} > 0.0205 \frac{N_{Re_j} N_{Pr_{j,l}}}{\sqrt{N_{We_j}}} \left( \frac{d_j (P_{j,l} - P_{sat})}{\sigma} \right)^{5/2} \tag{23}$$

This assumes that radial heat transfer in the jet is dominated by conduction. This condition suggests that a sudden transition temperature or a critical superheat value is required for thermal breakup to take place.

Bushnell and Gooderum [3] conducted experiments with water where atomization was induced by flowing water at ambient pressure into an evacuated chamber. They conducted experiments with orifice diameters ranging from 0.01 to 0.04 inches and reported a sudden transition to atomization. They correlated their results with superheat. For the experiments with 0.01 and 0.02 inch orifices,

$$\frac{(T_{sh} - T_{sat})}{T_{sh}} = 0.10 \tag{24}$$

and for 0.03 and 0.04 inch orifices:

$$\frac{(T_{sh} - T_{sat})}{T_{sh}} = 0.07 \tag{25}$$

Brown and York [2] conducted experiments with water and freon and reported that a critical superheat exists, beyond which the liquid atomized into fine droplets. The diameters considered by Brown and York varied from 0.02 to 0.08 inches.

Recent large scale experimental data pertinent to liquid aerosolization and rainout are summarized in [12]. The data is also reported by Lantzy [13], and the Center for Chemical Process Safety (CCPS) [14] [15]. Reference [12] summarizes the liquid capture (rainout) data obtained under different storage conditions of temperature and pressure for chlorine, freon-11, water, cyclohexane, and monomethylamine. Total liquid capture was not observed at low superheats for any of

Figure 4: Dependence of bubble growth rate on available energy

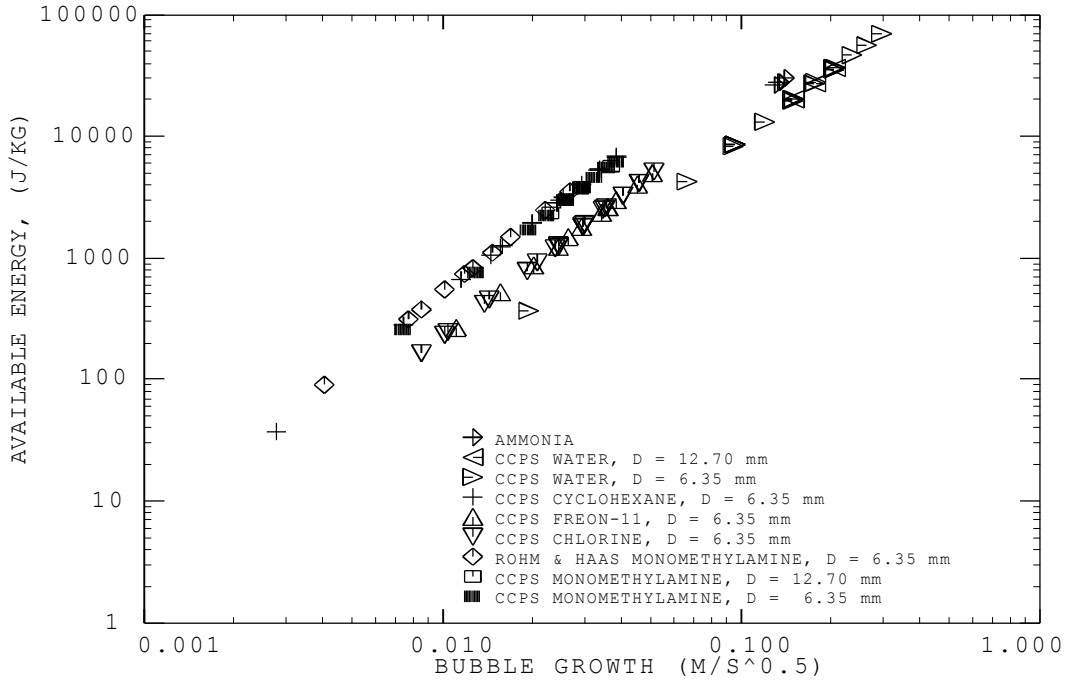


the materials. This is attributed to droplet evaporation and dynamics. The effect of droplet evaporation is shown to be significant for materials with low normal boiling points such as chlorine.

It is apparent that at large orifice diameters the flashing process plays an important role in the aerosolization of the liquid droplets. Flashing is the conversion of internal energy stored in the liquid to available energy by which the liquid is vaporized. Therefore, it is reasonable to assume that the aerosolized liquid fraction of superheated liquid releases should correlate with the total amount of available energy.

It is interesting to note that the transition region to flash atomization reported at small orifice diameters is much smaller than the transition regions reported by Lantzy [13] and subsequently by CCPS [14] [15] with 0.25 and 0.5 inch diameters.

Figure 4 shows the calculated values of available energy for the data summarized in reference [12] plotted against the bubble growth rate. It indicates that bubble growth is dominated by the amount of energy available in the liquid, $A_E$. Here, $A_E$ is the difference in internal energies between the initial and the final state minus the work done by expansion from the release pressure to ambient pressure.

We propose the following modification to the Weber number criteria for the calculation of a stable droplet diameter based on available energy:

$$N'_{We} = 2\frac{\rho_v A_E d_d}{\sigma_d} \tag{26}$$

The available energy per unit mass, $A_E$, represents the difference in internal energy of the fluid

Figure 5: Best fit modified Weber number values as a function of normal boiling point

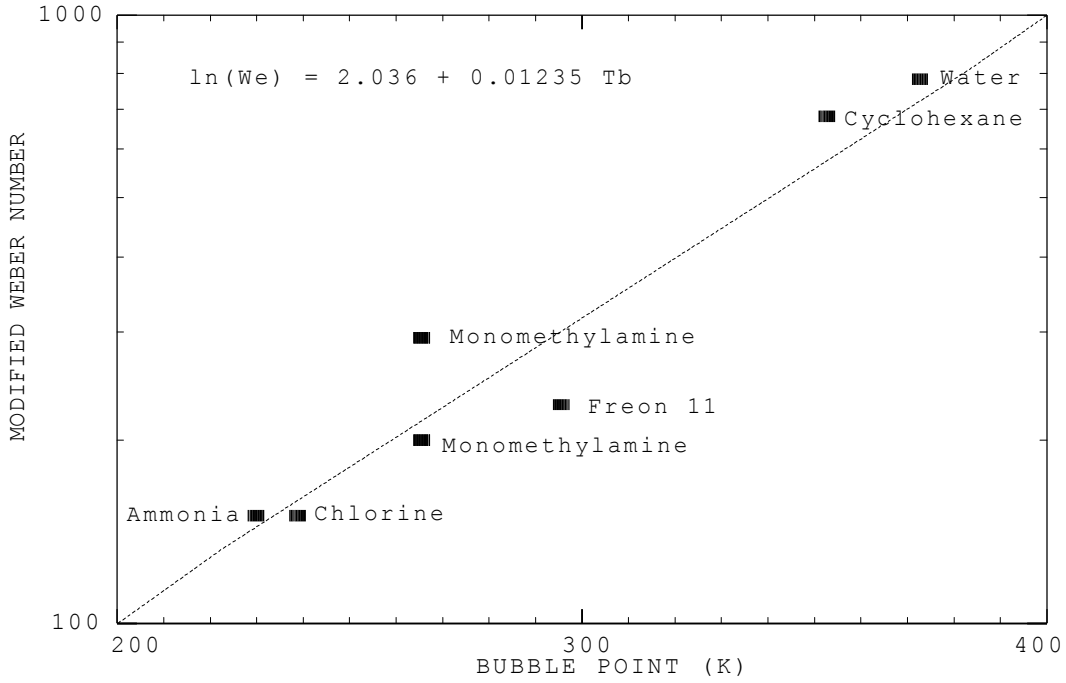


between the initial and final states. This represents the total amount of energy available for heat transfer, turbulence, etc. The maximum stable droplet diameter is proportional to $A_E$ and $\sigma_d/\rho_v$:

$$d_{d,\max} = f\left(\left[\frac{\sigma_d}{\rho_s}\right]^1 A_E^{-1}\right) \tag{27}$$

Critical values for $N'_{We}$ that reproduce the aerosol capture data reported by Lantzy and CCPS are shown in Figure 5.

It is interesting to note that Hinze [4] correlated the maximum stable droplet diameter at zero relative velocity where breakup is controlled by turbulence to power dissipated per unit mass:

$$d_{d,\max} = f\left(\left[\frac{\sigma_d}{\rho_s}\right]^{3/5} E^{-2/5}\right) \tag{28}$$

where $E$ is the power dissipated per unit mass. Equation 26 is similar in concept.

Figure 3 illustrates the dependence of the maximum stable droplet diameter on available energy and surface tension. Larger values of surface tension will lead to the formation of larger droplets while larger values of available energy will lead to the formation of smaller droplets.

# Aerosolization Parameters

The analysis of breakup mechanisms presented in the previous section indicates that the maximum stable droplet diameter depends on the following quantities:

- surface tension,
- viscosity,
- available energy, i.e. bubble growth rate, saturation temperature, bubble point, etc.

Modification of these key properties such that the maximum stable droplet diameter is increased will lead to more rainout. Larger droplets are less likely to be re-entrained into the jet because of their size. Larger droplets will exhibit less evaporative losses than smaller droplets because of the large difference in surface to volume ratio and the decreased residence time caused by larger terminal settling velocities. Droplet evaporation is very sensitive to drop size, especially in the region of droplet sizes between 200 and 400 microns. This is shown in Figure 8.

# Additive Technology

In 1991, Dr. George A. Olah, Director of the Loker Hydrocarbon Research Institute at the University of Southern California, was issued a patent [16] titled ”Environmentally Safe Catalytic Alkylation Using Liquid Onium Poly(Hydrogen Fluorides)”. This invention describes a process for alkylating an aliphatic hydrocarbon with an alkyl hydrocarbon in the presence of a liquid onium polyhydrogen fluoride complex as the reaction medium. Some examples of polyhydrogen fluoride complexes (MHF) include ammonia, methylamines, ethylamines, propylamines, butylamines, pyridine, and picolines. The concentration of the amine components of the MHF complex is between 5 to 30 wt %.

The MHF complex reduces the tendency of an aerosol/additive release to form an aerosol by two mechanisms. First, the Olah patent illustrates the concept that a reaction is occurring between the hydrofluoric acid and the additive to form a polyhydrogen fluoride complex. The polyhydrogen fluoride complex contains a long chain consisting of strongly associated HF molecules. This reduces the tendency of the HF molecules to form an aerosol upon a superheated, pressurized release. Second, the physical vapor pressure of the polyhydrogen fluoride complex is lower than that of anhydrous AHF.

The advantages of using an additive are mainly source term related, i.e., vapor flash fraction and fraction of aerosolized liquid are reduced because of lower internal energy content of the liquid and modified transport properties such as surface tension and viscosity (see Table 1). For the same initial storage conditions, a stable additized HF droplet will have a diameter that is three times larger than that of HF. This is illustrated in Figures 1 and 3.

Table 1: Impact of additive of mixture transport and thermophysical properties. 20 C

| Mixture | $\mu/\mu_{HF}$ | $\sigma/\sigma_{HF}$ | $\rho/\rho_{HF}$ |
|---|---|---|---|
| Additive | 4.90 | 4.42 | 1.01 |
| Complex | 20.20 | 6.56 | 1.23 |
| 15 % Complex in HF | 1.90 | 2.67 | 1.15 |

# HF Tests

Previous HF testing concentrated on examining the basic phenomena controlling a flashing release of AHF and hydrocarbons, or the mitigation of an AHF release using water spray systems. Two large-scale outdoor test series were conducted, the Goldfish series and the Hawk series. Smaller, laboratory scale testing was conducted to assess the effectiveness of passive mitigation measures such as the use of a less volatile modified hydrofluoric acid (MHF) alkylation catalyst.

During the summer of 1986, Amoco Oil Company and Lawrence Livermore National Laboratory conducted a series of six experiments involving large scale atmospheric releases of AHF. This series of atmospheric dispersion experiments is known as the Goldfish Test Series [1], [17], [18] (also see [19]). These experiments were conducted at the Department of Energy Liquefied Gaseous Fuels Facility which is located on the Nevada Test Site at Frenchman's Flats.

The tests were conducted because considerable uncertainty existed as to the amount of material that might become airborne after a release of superheated AHF. This uncertainty resulted in a large uncertainty in the size of the downwind hazard zone from an accidental release of AHF.

The Goldfish tests demonstrated that flashing occurred for accidental releases of AHF at typical alkylation unit temperatures and pressures (above the boiling point). No liquid rainout of AHF was observed. All of the released material became airborne as an aerosol-vapor cloud. The resulting cloud was cold and much denser than ambient air. The entire release remained cold, dense and compact as it initially moved downwind. At approximately 700 to 1000 meters downwind AHF cloud breakup was observed.

# 1990 Laboratory Tests

While the Hawk Test Series showed that water sprays can be highly effective in mitigating an accidental AHF release, the delays in activating water sprays were thought to have a potentially detrimental effect on controlling an AHF release. In late 1989, Texaco initiated research into passive means of mitigation. After evaluating patent literature and other sources, several groups of chemicals were identified to react with AHF to form a modified hydrofluoric acid (MHF) complex. The objective of using a MHF alkylation catalyst was to reduce the vapor pressure and aerosol forming tendencies of the AHF alkylation catalyst, while still maintaining kinetic activity and product selectivity for the alkylation reaction.

In February of 1990, Texaco and Mobil jointly carried out laboratory experiments at Mobil's Princeton Laboratories to evaluate the aerosol forming tendencies of 17 different MHF complexes. This joint effort was successful in identifying additives that would suppress the HF aerosol formation, but these additives failed the kinetic studies and would not support the alkylation reaction.

## 1991-1993 Laboratory Tests

During 1991-1993, two small scale release chambers were designed and built to confirm the aerosol reduction capability of HF complexing materials cited in the Olah patent. The fraction of the release of MHF that formed a liquid pool was quantified at different additive concentrations and release conditions. These experiments were not designed to obtain absolute liquid rainout values, but to rank the relative liquid rainout of many different additives. Many factors were not accounted for with these laboratory tests including wind velocity, amount of air entrainment, humidity, time of flight, release geometry, release orifice, and ambient temperature.

The baseline experiment of an AHF release at 318 K and 791 kPa (100 psig) averaged 0.9 wt % liquid rainout. This corresponds to similar results obtained in the 1986 HF Hawk Test Series. Approximately 15 different additives were tested, and some produced greater than 90 wt % liquid rainout. These experiments confirmed the the Olah technology is effective in reducing the quantity of hydrofluoric acid (HF) that becomes airborne; thereby significantly reducing the potential environmental hazard of an HF plume traveling downwind if an episodic release were to occur.

## 1992-1993 QUEST Experiments

In the spring of 1992, a Mobil Research and Development Company designed flow chamber was built at the Quest Consultants test site near Newcastle, Oklahoma. The chamber was designed to study the effect of several variables on the liquid rainout or pooling of HF/additive mixtures and anhydrous HF releases. The effects of orifice size, release temperature and pressure, concentration of additive, effect of dissolved hydrocarbons, and the effect of evaporation after pooling could be evaluated using the installed equipment.

The chamber was constructed of prefabricated resin-coated plywood panels and erected on a leveled C-channel steel footing at the site. Temperature controlled liquid for each test was released from a pressurized vessel through an orifice into the chamber. The release vessel was supported by load cells so that the vessel could be weighed continuously. Eight collection pans, each 15 ft wide and 10 ft long, were set side by side inside the flow chamber. Liquid collected in the pans was drained into a collection tank mounted on load cells. The weight of the release vessel and capture tank were monitored and recorded during each test. Airborne material not collected in the capture pans was removed in a two-stage water scrubber. Each scrubber stage had a collection sump and spray pump for recirculation of the water to the spray header. The

scrubber system was located directly downstream of the capture pans. HF detectors were set up downwind from the flow chamber to monitor the concentration of unmitigated fumes.

For each test, a material balance was calculated for each of the liquid components: HF, additive, and water. Analyses of the weighed liquid dropout permitted quantification of the disproportionate loss of HF and gain of water from the liquid released. Sump levels and sump water analyses provided a nearly complete closure of the material balance, with only minor quantities escaping to the atmosphere.

The major processing areas at the site included:

- Flow chamber
- HF storage, transfer, and conditioning
- Liquid capture and weighing
- HF scrubbing
- Chemical laboratory

A Simplified flow diagram for the test equipment is shown in Figure 6 (see [20]).

## Flow Chamber

The flow chamber was designed to have a high degree of turbulence, similar to the turbulence found at an industrial location. Fans at the end of the chamber provided an average air flow rate of 5 mph inside the chamber. The chamber was made of 1/2-inch resin-coated HDO plywood 8 ft by 16 ft high. Inside the chamber, eight collection pans, each 10 ft x 15 ft, were set up side by side to cover a downwind length of 80 ft from the front of the chamber. The pans extended from one side of the chamber to the other side with approximately 1/2 inch of space on each side. The pans had sloping bottoms and a 3/4 inch drain line. Each drain line had a sample valve so that each pan's contents could be separately sampled, if required. The pans were loosely lined with a 4 mil polyethylene liner secured to each pan with roof caulking. The polyethylene liner minimized the area where HF could contact the steel pan surfaces.

## HF Storage, Transfer, and Conditioning

Anhydrous HF, purchased from Allied Signal, was delivered in one ton cylinders. Each cylinder contained 1,300 lb of HF. Four cylinders were connected through a common manifold. The cylinders were used one at a time to charge HF through 1/2-inch flexible, teflon lined, metal hose into the transfer pipe manifold.

The transfer of HF from a cylinder to the release tank (F-5) was done by pressurizing the cylinder to about 70 psig with nitrogen and forcing the liquid HF through the manifold and piping to F-5.

Figure 6: Simplified flow diagram of the HF test facility

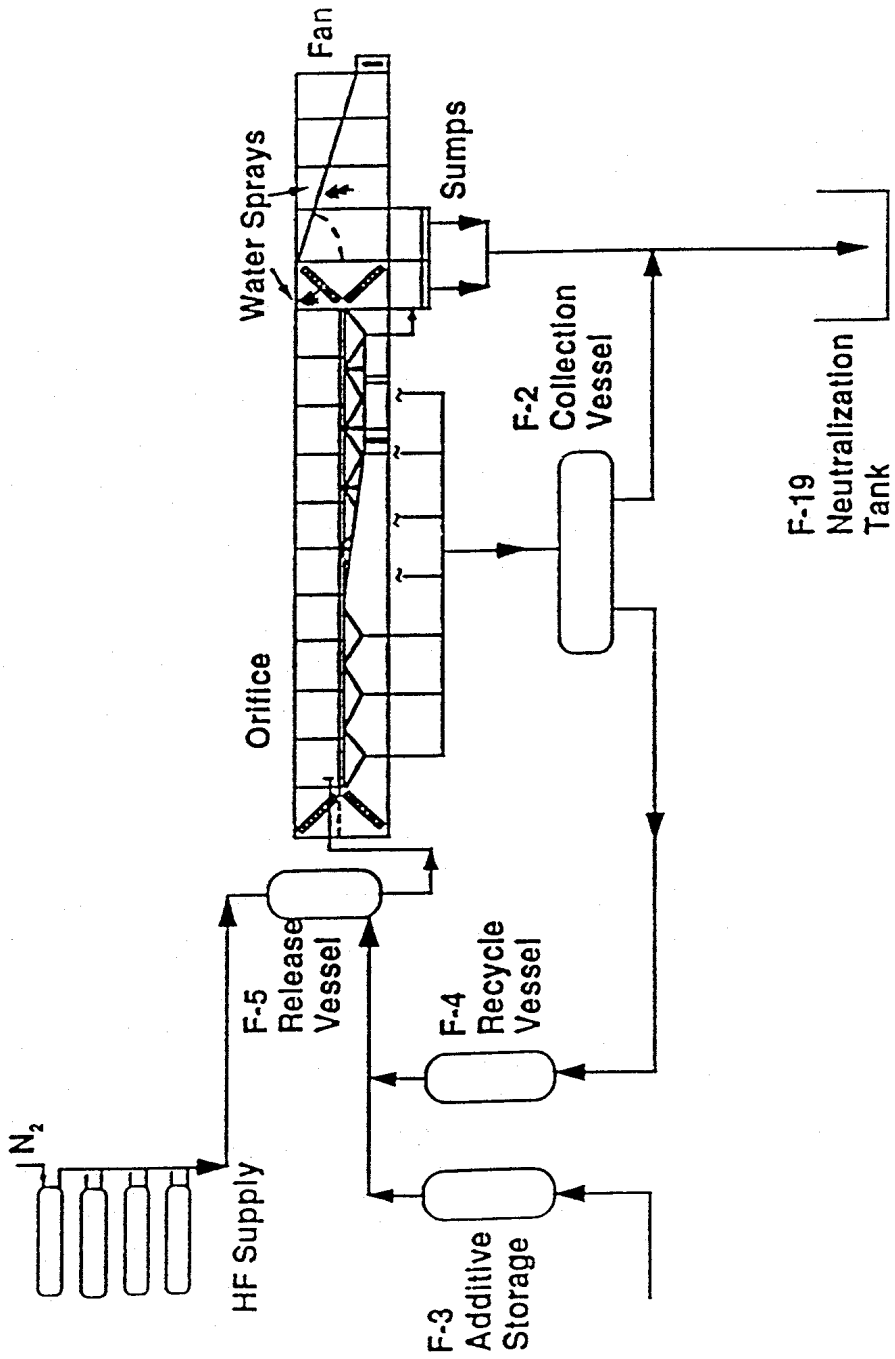

After transfer of HF, the manifold and transfer piping were purged with nitrogen. The weight of material in F-5 was measured using 3 load cells that supported the entire vessel weight. The combined load cell capacity was 7,500 lbs.

Once charged to F-5, the HF or HF/additive mixture was circulated by a circulation pump through a shell and tube heat exchanger. Pressure on F-1 was kept slightly higher than the suction side of the pump. The heat exchanger was a shell-and-tube design, with the cooling/heating fluid on the tube side and the HF/additive mixture on the shell side. It had a heat transfer area of 103 ft2, shell side pressure rating of 225 psig, and tube side pressure rating of 150 psig. Refrigeration was provided by a glycol/water chiller unit of 120,000 Btu/hr capacity manufactured by TUI Industries, Anaheim, California. Heat was supplied by a commercial electric water heater manufactured by Prestige, with a 92,200 Btu/hr capacity.

## Liquid Capture and Weighing Area

The liquid collected in the flow chamber capture pans was gravity drained to a 1000 gal. capacity capture tank (F-2). The drain lines from each capture pan were constructed of 3/4-inch PVC piping. The drain lines connected into a 1 1/2-inch manifold, the manifold to the capture tank. F-2 was located in a 24-inch deep concrete pit. This allowed an adequate slope on the drain lines to the tank and simultaneously provided a sump for the tank contents. The tank was mounted on 4 load cells with a combined capacity of 16,000 lbs.

During collection, the capture tank was vented to the inside of the flow chamber through a 2-inch vent line. The tank was equipped with a thermocouple, a differential pressure transmitter, and a pressure indicator. Sampling of the tank contents was done at a sample port on the tank discharge piping. Piping was provided to route the tank contents to either the neutralization tank (F-19), the recycle tank (F-4), or back to the capture pans.

## HF Scrubbing

A water scrubbing system was used to remove HF from the air flowing in the chamber. This allowed HF/additive releases greater than 25 lb/sec to be made while remaining within the permitted release rate of HF to the atmosphere. The scrubbing system consisted of two separate water sprays installed sequentially at the end of the flow chamber. The sprays were constructed of 4-inch schedule 80 PVC piping with eight spray nozzles each, mounted on 2 ft centers, in a horizontal run across the ceiling of the flow chamber. The nozzles, constructed of 316 ss, were mounted directly into drilled and tapped holes in the PVC pipe. The nozzles were supplied by Bete Fog Nozzle, Inc, Type TF32FCN full cone, and rated to give a flow of 52 gpm at 100 psig water pressure. Nozzles in the spray nearest the end of the capture system (north end) pointed straight down, while the header of the other spray (nearest chamber entrance) was turned 45ø upwind to reduce water loss past the edges of the sump. Two pumps with a nominal capacity of 500 gpm at 100 psig discharge, were used to recirculate spray water from the individual sumps

through the spray headers.

## Chemical Laboratory

A chemical laboratory was located onsite which allowed for rapid analysis of the test and neutralization samples. The chemical laboratory was set up to analyze samples from the release tank (F-5), capture tank (F-2), and water spray sumps for HF, additive, and water. Results from the analytical measurements were used to calculate the effectiveness of the additive in reducing airborne HF and material balance closure.

For the release and capture streams, the HF concentration was determined by neutralization and subsequent back-titration with caustic. The errors from this technique are due primarily to the slight loss of HF vapor during the first neutralization step. The additive concentrations were measured using a gas chromatagraph. The water concentrations were determined using the technique of Karl-Fischer titration. The errors in this analysis are attributed to the instrument error during the titration step, the error in establishing the titer value of the hydranal reagent, and the slight loss of HF vapor during the transfer to the titration vessel.

## Jet Dispersion For Flashing Liquids

This section will establish a model by which the fraction of liquid rainout can be estimated for a wide range of storage temperatures and pressures. Figure 7 illustrates such a model which consists of four major steps:

1. source term characterization,
2. aerosol formation,
3. droplet evaporation, and
4. jet conservation laws.

In source term characterization the source geometry, release type, and initial conditions are established. Source geometries include leakage through cracks and openings, emergency relief, and pipe ruptures. Release types include gas/vapor, subcooled liquid, saturated flashing liquid and two-phase flow. Initial conditions established include release mass flow rate, temperature, flash fraction, expanded diameter, etc.

## Droplet Evaporation

Droplet evaporation can be a significant factor in determining the fraction of rained-out liquid to reach the surface following an elevated continuous release of a superheated liquid. Droplet

Figure 7: Model structure

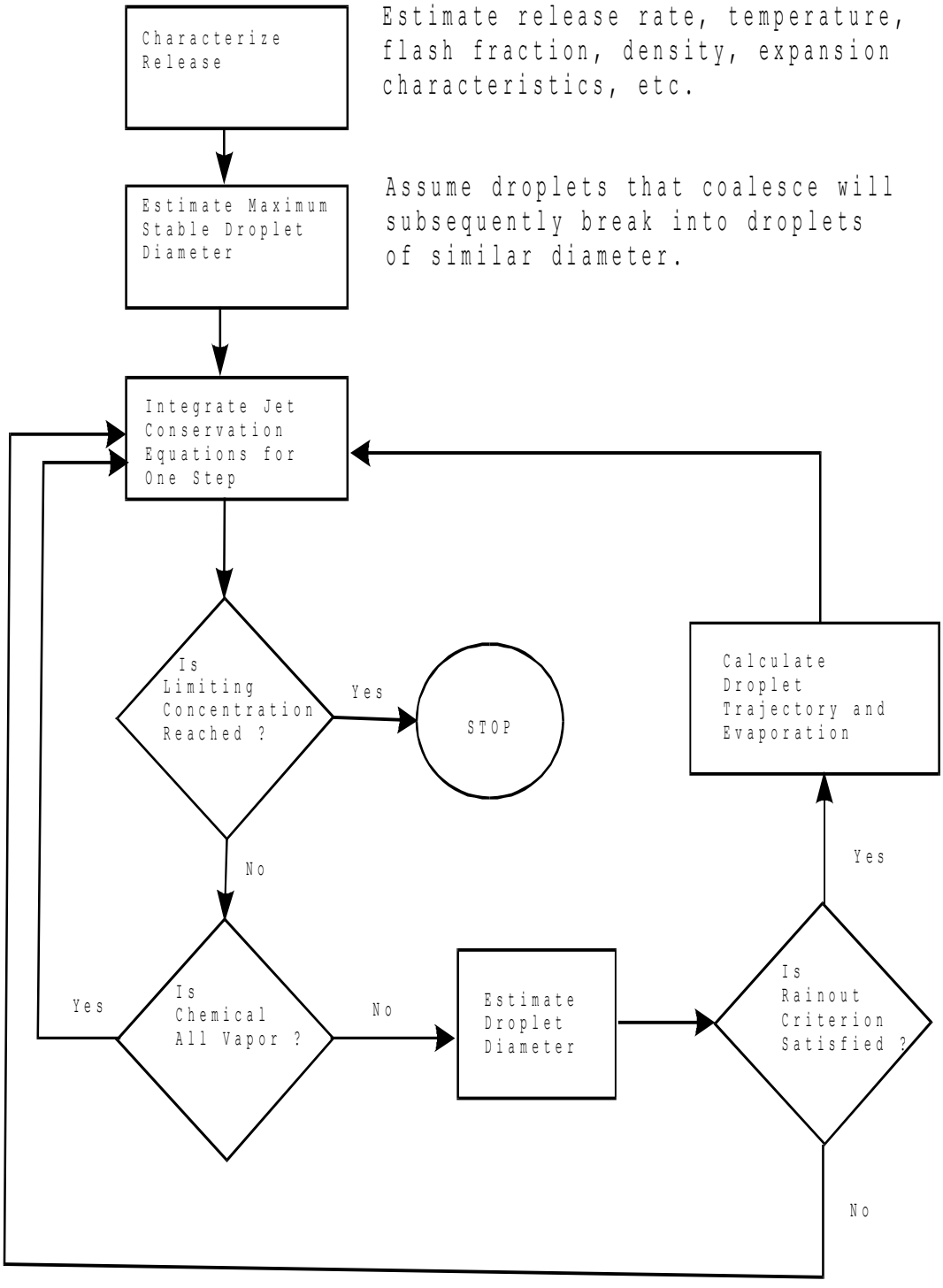

evaporation is significant for materials with low boiling points at ambient pressure. In this section a model based on conservation laws which predicts the temperature, trajectory, and mass evaporated for a single falling liquid droplet will be derived. This model is similar to the models developed by Papadourakis et al. [21], Vesala et al. [22], Kukkonen et al. [23], [24], [25], and Woodward and Papadourakis [26].

Consider an evaporating spherical droplet moving in a gas medium where the evaporating mass is diffusing through the vapor phase. The change of droplet mass is a function of the mass transfer coefficient, the droplet surface area, and concentration difference:

$$\frac{dM_d}{dt} = -K_s A_d \left[C_d - C_s\right] \tag{29}$$

where $A_d$ is the surface area of the droplet and is equal to:

$$A_d = \pi d_d^2 \tag{30}$$

Equation 29 is equivalent to:

$$\frac{dM_d}{dt} = -A_d K_s \rho_{d_s} \chi_1 \chi_2 \ln\left[\frac{1 - P_{d_s}/P_s}{1 - P_d/P_s}\right] \tag{31}$$

where $\rho_{d_s}$ is the gas density of the droplet evaluated at ambient conditions, $P_{d_s}$ is the partial pressure of the droplet material in the gas phase, and $P_d$ is the saturation pressure at the droplet surface. If the drop is evaporating in pure air, then $P_{d_s} = 0$. The vapor density of the drop is calculated using the ideal gas law:

$$\rho_{d_s} = \frac{P_s M_{w_d}}{R_g T_s} \tag{32}$$

$\chi_1$ and $\chi_2$ are correction factors for the temperature effect on diffusivity for Stefan flow and for temperature dependence of the diffusion coefficients:

$$\chi_1 = 1 + \frac{P_d + P_{d_s}}{2P_s} \tag{33}$$

$$\chi_2 = \frac{T_s - T_d}{T_s^{\chi_3 - 1}} \frac{2 - \chi_3}{T_s^{2-\chi_3} - T_d^{2-\chi_3}} \tag{34}$$

$$\chi_3 = 1.8 \tag{35}$$

Stefan flow is defined as the additional mass flux leaving the surface of the droplet due to the relative motion of the center of mass of the air-vapor mixture to the droplet surface (see Wagner [27]).

The mass transfer coefficient can be calculated from empirical correlations relating the Sherwood number to the drop's Reynolds and Schmidt numbers:

$$K_s = \frac{D_{ds} N_{Sh}}{d_d} \tag{36}$$

$$N_{Sh} = \alpha + \beta N_{Re}^{1/2} N_{Sc}^{1/3} \tag{37}$$

where $\alpha$ and $\beta$ are constants having the values of 2 and 0.6 respectively. The Sherwood number is the ratio of total mass transfer to diffusive mass transfer. The Schmidt number is defined as the ratio of momentum to mass diffusivity:

$$N_{Sc} = \frac{\mu_s}{\rho_s D_{ds}} \tag{38}$$

Assuming that no kinetic energy is converted into thermal energy, an overall heat balance for the droplet can be written as follows:

$$\frac{dM_d H_{d_l}}{dt} = A_d h \left(T_s - T_d\right) + \frac{dM_d}{dt} H_{d_v} + A_d \sigma \left[(1-r)T_s^4 - eT_d^4\right] \tag{39}$$

where $\sigma$ is the Stephan-Boltzman constant which is equal to $5.6667 \times 10^{-8}$ $\mathrm{J/m^2/s/K^4}$. The variables $e$ and $r$ represent the droplet surface emissivity and reflectivity. The first term on the right accounts for convective heat transfer, the second term accounts for evaporative cooling, and the last term accounts for radiative heat transfer.

Assuming constant heat capacities for the droplet material and using the same reference temperature for both vapor and liquid, the conservation of energy equation can be re-written as:

$$\begin{aligned} \frac{dT_d}{dt} &= \frac{1}{M_d C_{p_{d,l}}} \Big[ A_d h \left(T_s - T_d\right) + A_d \sigma \left( (1-r)T_s^4 - eT_d^4 \right) \\ &+ \frac{dM_d}{dt} \left[ \underline{\lambda}_{d_{vl}} + (C_{p_{d,v}} - C_{p_{d,l}})(T_d - T_0) \right] \Big] \end{aligned} \tag{40}$$

where, the liquid and vapor enthalpies are given by:

$$H_{d_l} = C_{p_{d,l}} \left[T - T_0\right] + \underline{\lambda}_{d_{vl}} \tag{41}$$

$$H_{d_v} = C_{p_{d,v}} \left[T - T_0\right] \tag{42}$$

In a similar fashion to mass transfer, the coefficient for heat transfer can be calculated from the Nusselt number which is defined as the ratio of total heat flux to conductive heat flux:

$$N_{Nu} = \frac{h d_d}{k_s} \tag{43}$$

The Nusselt number is calculated using the empirical relation:

$$N_{Nu} = \alpha + \beta N_{Re}^{1/2} N_{Pr}^{1/3} \tag{44}$$

where $N_{Pr}$ is the Prandtl number and is defined as:

$$N_{Pr} = \frac{C_{p_s} \mu_s}{k_s M_w} \tag{45}$$

The droplet's momentum must be conserved in both the vertical and horizontal directions. The change of momentum in the horizontal direction is:

$$\frac{d\left(M_d u_{d,x}\right)}{dt} = u_{d,x}\frac{dM_d}{dt} - C_D\frac{A_d}{4}\frac{1}{2}\rho_s u_{d,x} u_d \tag{46}$$

where $u_d$ is defined by:

$$u_d = \sqrt{u_{d,x}^2 + u_{d,z}^2} \tag{47}$$

The first term of the right hand side of Equation 46 represents the momentum lost due to mass evaporated, and the second term represents momentum change because of the drag force.

Equation 46 is re-written to represent the change in the droplet horizontal velocity component:

$$\frac{du_{d,x}}{dt} = -\frac{1}{M_d}C_D\frac{A_d}{4}\frac{1}{2}\rho_s u_{d,x} u_d \tag{48}$$

The conservation of droplet momentum in the vertical direction is:

$$\frac{d\left(M_d u_{d,z}\right)}{dt} = u_{d,z}\frac{dM_d}{dt} + gM_d\frac{\rho_s}{\rho_{d,l}} - gM_d - C_D\frac{A_d}{4}\frac{1}{2}\rho_s u_{d,z} u_d \tag{49}$$

The first term on the right hand side represents momentum lost due to mass evaporated, the second term represents the buoyancy force acting on the droplet, the third represents the droplet's weight, and the last term represents the vertical component of the drag force.

Equation 49 is re-written to represent the change in the droplet vertical velocity component:

$$\frac{du_{d,z}}{dt} = g\left(\frac{\rho_s}{\rho_{d,l}} - 1\right) - \frac{C_D}{M_d}\frac{A_d}{4}\frac{1}{2}\rho_s u_{d,z} u_d \tag{50}$$

Note the $u_{d,z}$ is positive if the droplet is moving upwards and negative if the droplet is falling.

The droplet position at any time is represented by the following trajectory equations:

$$\frac{dX_d}{dt} = u_{d,x} + U_w \tag{51}$$

$$\frac{dZ_d}{dt} = u_{d,z} \tag{52}$$

Figure 8 shows the effect of droplet diameter and boiling point on evaporation for ammonia, methylamine, cyclohexane, water, freon-11, and chlorine. The droplet evaporation was calculated by assuming a freely falling droplet at its boiling point using an ambient temperature of 304 K, an ambient pressure of 90000 Pa, a release elevation of 1.22 m, a wind speed of 5 m/s at 3 m elevation and a power law constant of 1/7.

Figure 8: Rainout as a function of droplet diameter

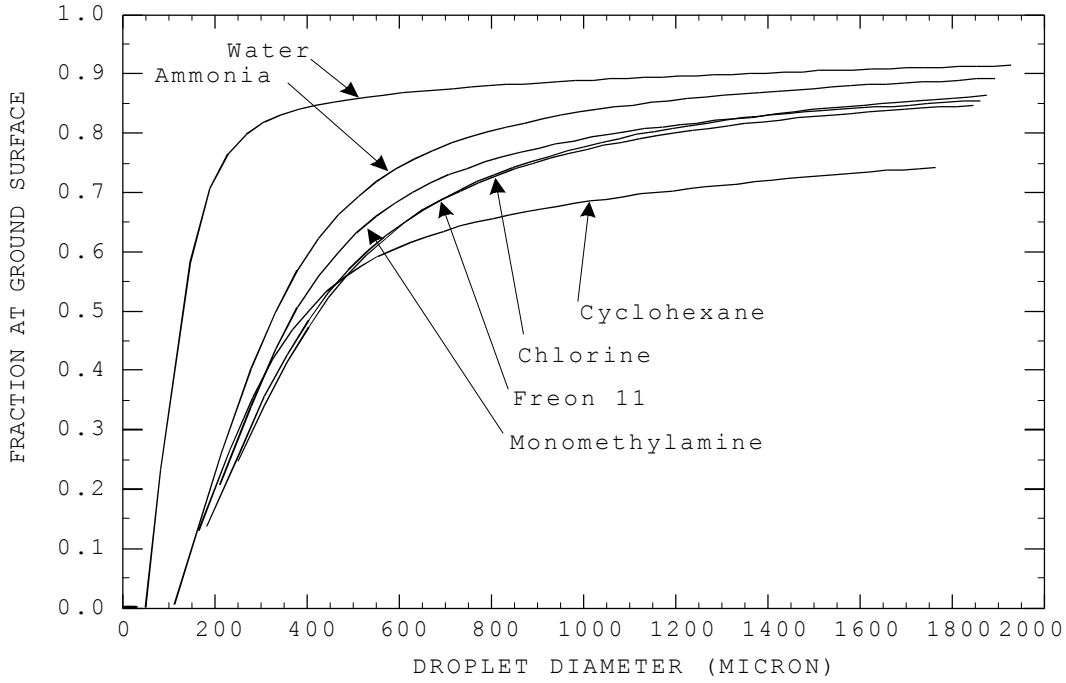


The graph illustrates the importance of droplet evaporation on liquid rainout when droplet diameters are less than 400 microns. Under the same conditions, CCPS reported capture data that is consistent with the model predictions. For chlorine the maximum liquid capture was about 20 % while for water it was about 87 %.

The slope of the curves shown in Figure 8 illustrate the sensitivity of droplet evaporation to increasing surface to volume ratio with decreasing droplet diameter. This indicates that an accurate estimate of droplet diameter is required to predict rainout for typical pressurized liquid releases.

The equations presented earlier for droplet evaporation of a single component, can be extended to cover a droplet containing a liquid mixture with nonideal behavior. In order to simplify the notation, we reformulate the droplet equations as a function of number of moles in the liquid phase of species $i$:

$$\frac{dn_{d,i}}{dt} = -\frac{dn_{d,i,out}}{dt} = -A_d K_{s,i} \chi_{1_i} \chi_2 \ln\left[\frac{1 - Y_{i,0}}{1 - Y_i^*}\right] \tag{53}$$

The vapor mole fraction in equilibrium with the liquid pool surface, $Y_i^*$, is given by the following equilibrium relation:

$$Y_i^* = \frac{\hat{\Phi}_{l,i} X_i}{\hat{\Phi}_{v,i}} \tag{54}$$

For ideal liquid and vapor phase behavior, $Y_i^*$ is given by:

$$Y_i^* = \frac{P_{sat,i} X_i}{P_s} \tag{55}$$

If the drop is evaporating in pure air, then $Y_{i,0} = 0$. $\chi_{1_i}$ is defined as:

$$\chi_{1_i} = 1 + \frac{Y_i^* + Y_{i,0}}{2} \tag{56}$$

The individual component mass transfer coefficient can be calculated from empirical correlations relating the Sherwood number to the drop's Reynolds and Schmidt numbers:

$$K_{s,i} = \frac{D_{ds_i} N_{Sh_i}}{d_d} \tag{57}$$

$$N_{Sh_i} = \alpha + \beta N_{Re_m}^{1/2} N_{Sc_i}^{1/3} \tag{58}$$

where $\alpha$ and $\beta$ are constants having the values of 2 and 0.6 respectively. The Sherwood number is the ratio of total mass transfer to diffusive mass transfer. The Schmidt number is defined as the ratio of momentum to mass diffusivity:

$$N_{Sc_i} = \frac{\mu_s}{\rho_s D_{ds_i}} \tag{59}$$

The droplet temperature can be calculated using a comprehensive energy balance which accounts for heat loss due to evaporation, heat exchange due to convection and radiation. The overall internal energy change of the liquid droplet is:

$$\frac{dT_l}{dt} = \frac{c}{a} \tag{60}$$

where $a$, and $c$ are constants defined as follows:

$$a = \sum_i^C n_i C_{v_i} + n_T \frac{\partial \Delta \underline{U}_l}{\partial T}$$

$$c = \frac{dQ}{dt} - \sum_i^C \left( \int_{T_{\text{ref}}}^T C_{v_i} dT + \Delta \underline{U}_l + n_T \frac{\partial \Delta U_l}{\partial n_i} \right) \frac{dn_{d,i}}{dt}$$

$$\frac{dQ}{dt} = A_d h \left(T_s - T_d\right) + A_d \sigma \left[(1-r) T_s^4 - e T_d^4\right] - \underline{H}_v \sum_i^C \frac{dn_{i,d,out}}{dt}$$

# Flashing Two-phase Jets

Ooms [28],[29] derived one-dimensional conservation laws to describe the dispersion of gaseous jets. In this section we present a similar analysis for two-phase flashing jets with the following additions/modifications:

- Physical equilibrium is considered, and
- the velocity, density, and temperature profiles are assumed to be top-hat.

For simplicity, the jet conservation equations are presented for a three components system: air, water, and the dispersing chemical. The equations can be easily modified to handle more components.

Air entrained in the jet as it flows through the atmosphere is accounted for by the following three mechanisms (see Abraham, 1970; Ooms, 1971; Ooms 1974; Hoult et al. 1969): ([30],[31],[28] and [29])

1. When the velocity of the jet is much larger than that of air, entrainment is assumed to be that of a free turbulent jet.
2. When velocity of the plume is approximately equal to that of air, entrainment is described as that of a cylindrical thermal plume in a stagnant atmosphere.
3. Turbulence of the atmosphere is also an important factor in calculating the amount of air entrained in the plume.

These three mechanisms are built into the following equation:

$$u_e = \alpha_1 \sqrt{\frac{\rho_m}{\rho_a}} |u - U_w \cos\theta| + \alpha_2 U_w \cos\theta |\sin\theta| + \alpha_3 u' \tag{61}$$

where $\alpha_1$ is the entrainment coefficient of a free jet (see Ricou and Spalding [32]), $\alpha_2$ is the entrainment coefficient for a line thermal, and $\alpha_3$ is the entrainment coefficient caused by turbulence. The coefficients were assigned values of 0.057, 0.5 and 1.0 by Ooms.

The mixture density $\rho_m$ is expressed as a function of the void fraction:

$$\rho_m = \alpha \rho_v + (1 - \alpha)\rho_l \tag{62}$$

Free-jet type entrainment is caused by the parallel component to the jet centerline of the velocity difference between the jet and ambient air. The normal component causes generation of the vortex pair in the wake disturbing the jet boundary and producing strong mixing. This becomes important when the jet is bent over and is approximated by the term $\alpha_2 \cos\theta$ (see Abraham, 1970; Ooms, 1972). ([30] and [28]).

The variable $u'$ represents the root mean squared turbulent fluctuation velocity because of atmospheric turbulence. A typical value suggested by Ooms for $u'$ is:

$$u' = (u_a^2)^{0.5} \tag{63}$$

where $u_a$ is the wind velocity fluctuation. Briggs (1969; 1972) ([33] [34]) showed that:

$$u' = (\epsilon b)^{1/3} \tag{64}$$

Table 2: Dispersion Coefficients Parameters

| *Stability Class* | | *p* | *m* | *q* | *n* |
|---|---|---|---|---|---|
| very unstable | A | 0.527 | 0.865 | 0.28 | 0.90 |
| unstable | B | 0.371 | 0.866 | 0.23 | 0.85 |
| slightly stable | C | 0.209 | 0.897 | 0.22 | 0.80 |
| neutral | D | 0.128 | 0.905 | 0.20 | 0.76 |
| stable | E | 0.098 | 0.902 | 0.15 | 0.73 |
| very stable | F | 0.065 | 0.902 | 0.12 | 0.67 |

where $\epsilon$ is the eddy energy dissipation. For a neutral atmosphere, Briggs assigns $\epsilon$ the value of $0.0677\frac{U_w}{y}$, for $y < 300$ m. For unstable atmosphere, Kaimal et al. [35] assign $\epsilon$ the value 0.004 and a value of 0 for stable atmosphere.

In the far field, entrainment is due solely to atmospheric turbulence. It can be estimated in a similar fashion to Gaussian models:

$$\alpha_3 u^{'} = \frac{db}{ds} U_w \cos\theta \tag{65}$$

Assuming a circular cross sectional area proportional to the product $\sigma_y \sigma_z$, $\alpha_3$ is equivalent to:

$$\alpha_3 = \frac{db}{ds} = \frac{b}{2}\frac{d}{ds}\ln\left(\sigma_y \sigma_z\right) \tag{66}$$

Typical values of the Gaussian standard deviations are reported as:

$$\sigma_y = p s^m \tag{67}$$

$$\sigma_z = q s^n \tag{68}$$

Then,

$$\alpha_3 = \frac{b}{2}\frac{m+n}{s} \tag{69}$$

Table 2 shows typical values of the parameters $p$, $q$, $m$ and $n$ for various atmospheric stability classes. Epstein et al. [36] used a similar approach to model jet growth in the far field due to atmospheric turbulence:

$$\alpha_3 u^{'} = \frac{U_w}{2b}\frac{d}{ds}\left(\sigma_y \sigma_z\right) \tag{70}$$

The equations representing the characteristics of the jet are as follows:

**Jet Z-coordinate**

$$\frac{dZ}{ds} = \sin\theta \tag{71}$$

**Jet X-coordinate**

$$\frac{dX}{ds} = \cos\theta \tag{72}$$

**Jet area**

$$\frac{dA}{ds} - 2\pi b = 0 \tag{73}$$

**Conservation of liquid mass**

$$\frac{dm_T}{ds} - M_{w_w}\frac{dn_w}{ds} - M_{w_C}\frac{dn_C}{ds} = 0 \tag{74}$$

$$\frac{dn_T}{ds} - \frac{dn_w}{ds} - \frac{dn_C}{ds} = 0 \tag{75}$$

$$\frac{dm_T}{ds} - \frac{d}{ds}\rho_l u A\,(1-\alpha) = 0 \tag{76}$$

**Conservation of vapor mass**

$$\frac{dM_T}{ds} - M_{w_w}\frac{dN_w}{ds} - M_{w_C}\frac{dN_C}{ds} + M_{w_a}\frac{dN_a}{ds} = 0 \tag{77}$$

$$\frac{dN_T}{ds} - \frac{dN_w}{ds} - \frac{dN_C}{ds} - \frac{dN_a}{ds} = 0 \tag{78}$$

$$\frac{dM_T}{ds} - \frac{d}{ds}\rho_v u A\alpha = 0 \tag{79}$$

**Individual species**

$$\frac{dN_C}{ds} + \frac{dn_C}{ds} = 0 \tag{80}$$

$$\frac{dN_a}{ds} = \frac{2\pi b\rho_a u_e}{M_{w_a}}\frac{1}{1+\zeta} \tag{81}$$

$$\frac{dN_w}{ds} + \frac{dn_w}{ds} - \zeta\frac{dN_a}{ds} = 0 \tag{82}$$

where

$$\zeta = \frac{\frac{P_w}{P_a}\frac{\mathrm{RH}}{100}}{1 - \frac{P_w}{P_a}\frac{\mathrm{RH}}{100}} \tag{83}$$

**Energy**

$$H_a\frac{dN_a}{ds} + H_w\frac{dN_w}{ds} + H_C\frac{dN_C}{ds} + \left(H_w - \underline{\lambda}_{v,w}\right)\frac{dn_w}{ds} + \left(H_C - \underline{\lambda}_{v,c}\right)\frac{dn_C}{ds} \quad +$$
$$\left[N_aC_{p_a} + \left(N_C + n_C\right)C_{p_C} + \left(N_w + n_w\right)C_{p_w}\right]\frac{dT}{ds} - \left[H_a + H_w\zeta\right]\frac{dN_a}{ds} = 0 \tag{84}$$

**Momentum in X-Direction**

$$\frac{d}{ds}\left(M_T + m_T\right)u\cos\theta = C_D\pi b\rho_a U_w^2|\sin^3\theta| + 2\pi b\rho_{a,w}U_w u_e \tag{85}$$

where, $C_D$ is the drag coefficient with a default value of 0.3.

**Momentum in Z-Direction**

$$\frac{d}{ds}\left(M_T + m_T\right)u\sin\theta = Ag\left(\rho_a - \rho_m\right) - C_D\pi b\rho_a U_w^2\cos\theta\sin\theta|\sin\theta| \tag{86}$$

**Physical equilibrium**

Assuming ideal behavior in both the liquid and vapor phase, the equilibrium constants for water and the dispersing chemical are obtained from their partial pressures:

$$K_w = \frac{P_w}{P_a} = \exp\left[A_w + B_w/T\right] \tag{87}$$
$$K_C = \frac{P_C}{P_a} = \exp\left[A_C + B_C/T\right] \tag{88}$$

The vapor pressure curve used in the equilibrium equations implies a constant heat of vaporization. It can be shown that the equations representing jet equilibrium are:

$$\frac{d}{ds}n_TN_C - K_C\frac{d}{ds}N_Tn_C + \frac{n_CN_TK_CB_C}{T^2}\frac{dT}{ds} = 0 \tag{89}$$
$$\frac{d}{ds}n_TN_w - K_w\frac{d}{ds}N_Tn_w + \frac{n_wN_TK_wB_w}{T^2}\frac{dT}{ds} = 0 \tag{90}$$

The equations representing physical equilibria are simple and will not predict the vapor-liquid equilibrium (VLE) behavior of highly non-ideal systems accurately. However, the near field impact of such predictions on jet temperature and jet vapor/liquid ratio is not significant because of the rapid entrainment of air.

For reactive materials such as hydrogen fluoride, chemical equilibria must also be addressed. Simultaneous nonideal physical-chemical equilibrium can be calculated by direct minimization of the Gibbs free energy, as outlined by Saini [37]. Nonideal mixture behavior is represented by a modified Peng-Robinson equation of state (see Melhem et al. [38]).

Mathematically, the equilibrium problem is to minimize the total Gibbs free energy

$$G^t = \sum_{i=1}^{S} n_i \frac{G_i^\circ}{RT} + \sum_{i=1}^{N-S} \sum_{p=1}^{\pi} n_{ip} \left[ \frac{G_i^\circ}{RT} + \ln\left( P\phi_{ip} \frac{n_{ip}}{n_{Tp}} \right) \right] \tag{91}$$

subject to the equality constraints,

$$C_1 \equiv \sum_{i=1}^{S} a_{ki} n_i + \sum_{i=1}^{N-S} \sum_{p=1}^{\pi} a_{ki} n_{ip} = b_k \qquad k = 1, \ldots, R \tag{92}$$

and the inequality constraints,

$$C_2 \equiv n_i \geq 0 \qquad i = 1, \ldots, S, \ldots, N\pi \tag{93}$$

where $N$ the number of chemical species, $\pi$ is the number of phases, $S$ is the number of condensed solid species, $n_{ip}$ is the equilibrium number of moles of the $i$th species in phase $p$, $n_{Tp}$ is the total number of moles in phase $p$, $G_i^\circ$ is the standard Gibbs free energy of the $i$ species evaluated at the system temperature $T$, $P$ is the system pressure, $a_{ki}$ is the number of atoms of element $k$ in species $i$, $b_k$ is the number of gram-atoms of element $k$, and $R$ is the rank of the atom matrix (usually equal to the number of elements). The element abundance vector $\mathbf{b}$ is calculated as the product of the atom matrix $\mathbf{A}$ and the initial composition $\mathbf{n}^\circ$

$$\mathbf{A}\mathbf{n}^\circ = \mathbf{b} \tag{94}$$

The number of variables is equal to $((N - S) \times \pi + S)$, the number of equality constraints is equal to the rank of the atom matrix $R$, and the total number constraints is equal to the number of variables plus the number of equality constraints. The constrained Gibbs free energy minimization problem can be solved efficiently using successive quadratic programming (see Saini, 1988).

**HF Oligomerization**

HF oligomerization is represented by using a three oligomer representation, 1,2,6. Comparison of recent data with model predictions indicate that HF oligomerization can be effectively represented using a 1,2,6 model. Figures 9 and 10 compare the 1,2,6 model predictions with recent experimental data (see [39, 40, 41]) on density along several isotherms and the saturation curve.

These figures indicate that HF liquid at typical operating alkylation temperatures is largely hexamer. The vapor also contains a large fractio of hexamer. At reduced pressures, the vapor phase is largely made of monomer. Figure 11 illustrates the impact of pressure on monomer equilibrium mole fraction using our 1,2,6 model. This indicates that while the release starts out containing large amounts of hexamer, as air is entrained into the jet/cloud and the partial pressure of HF is reduced, monomer formation is favored.

Figure 9: Comparison of model predictions for vapor density with the data of Wilding et al.

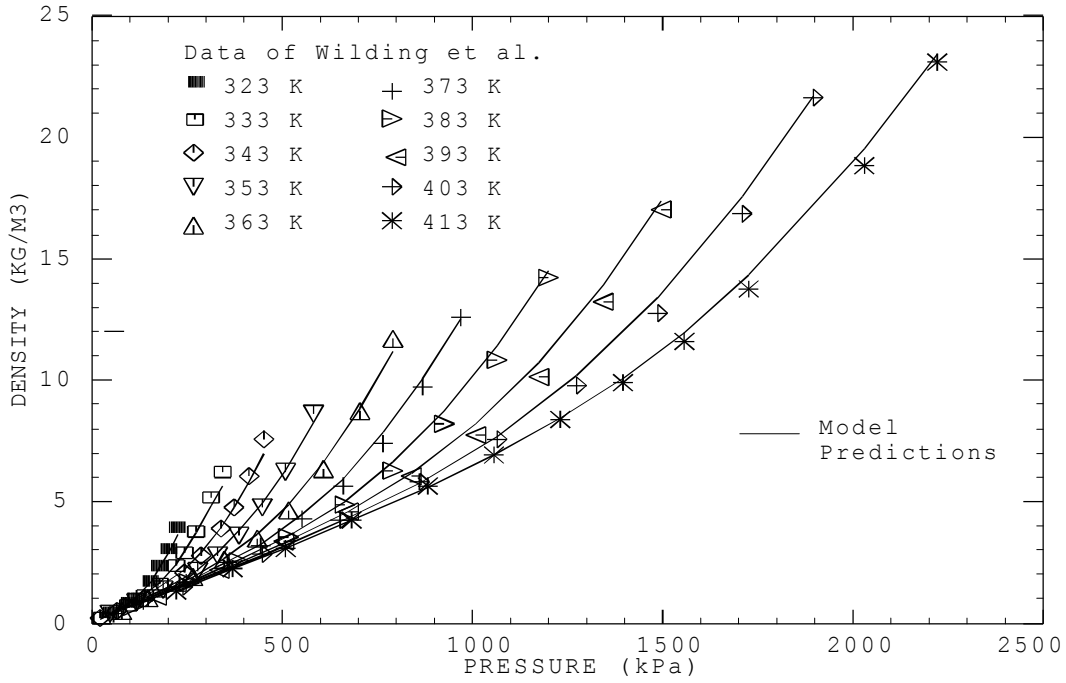


**Equation of state**

The ideal gas equation of state is used to represent the gas/vapor phase volumetric behavior:

$$\frac{d}{ds}\left[\rho_v T \frac{N_T}{M_T}\right] = 0 \tag{95}$$

A temperature dependent correlation is used to calculate saturated liquid densities:

$$\frac{d}{ds}\left[\frac{1}{\rho_l} - \frac{n_w v_w + n_C v_C}{m_T}\right] = 0 \tag{96}$$

where, $v_w$ and $v_C$ are the liquid molar volumes for water and the dispersing chemical. They are assumed to be a function of temperature only.

# Liquid Rainout

The criteria used to determine whether a drop of a given size will rain out is based on hydrodynamic considerations. The drop is considered to remain airborne (no rain-out) if the rate at which the jet expands by entrainment exceeds its terminal settling velocity:

$$u_j \frac{dR}{ds} > u_t \tag{97}$$

Figure 10: Comparison of model predictions for HF hexamer with the data of Gillespie et al. and the model of Twu et al.

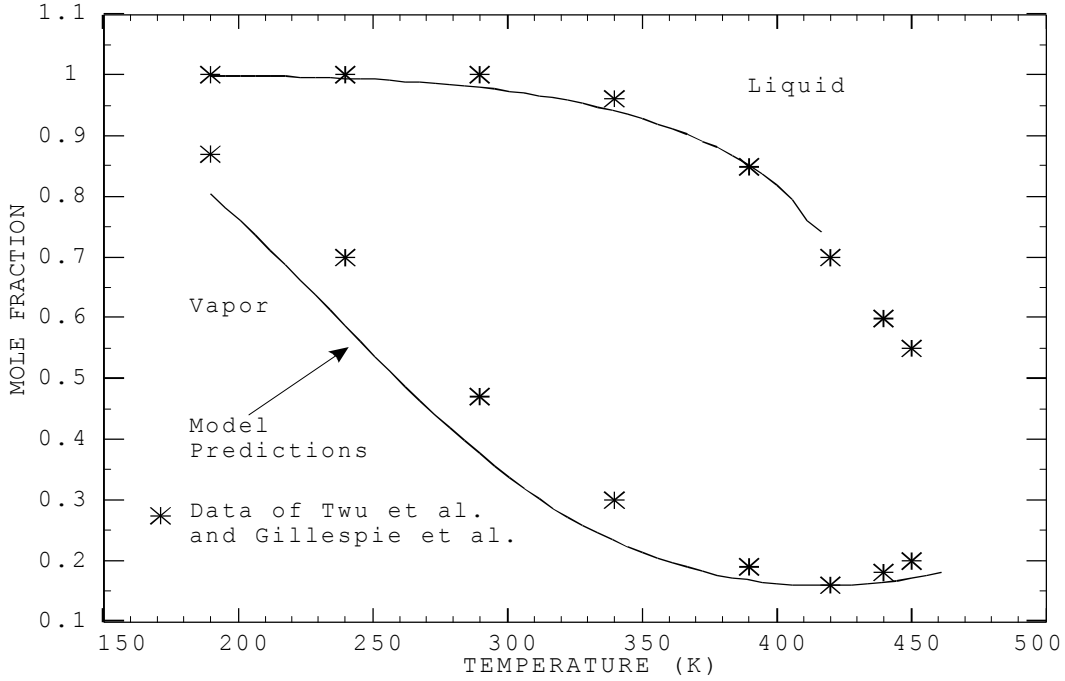


The droplet terminal settling velocity is given by Seinfeld [42]:

$$u_t = \sqrt{g\frac{4}{3}\frac{\rho_{d_l}}{\rho_s}\frac{d_d}{C_D}} \tag{98}$$

where $C_D$ is the drag coefficient and is given by the following expressions:

$$C_D = \frac{24}{N_{Re}} \quad , \mathrm{N_{Re}} < 0.1 \tag{99}$$

$$C_D = \frac{24}{N_{Re}}\left[1 + \frac{3}{16}N_{Re} + \frac{9}{160}N_{Re}^2\ln(2N_{Re})\right] \quad , 0.1 < \mathrm{N_{Re}} \quad 2 \tag{100}$$

$$C_D = \frac{24}{N_{Re}}\left[1 + 0.15N_{Re}^{0.687}\right] \quad , 2 \quad \mathrm{N_{Re}} < 500 \tag{101}$$

$$C_D = 0.44 \quad , 500 \quad \mathrm{N_{Re}} < 200,000 \tag{102}$$

$N_{Re}$ is the droplet Reynolds number and is based on the relative velocity, $u_{d,s}$, between the droplet and the surrounding medium:

$$N_{Re} = \frac{d_d|u_{d_s}|\rho_s}{\mu_s} \tag{103}$$

Figure 11: Model predictions for HF monomer fraction as a function of pressure. Balance contains hexamer and small amounts of dimer.

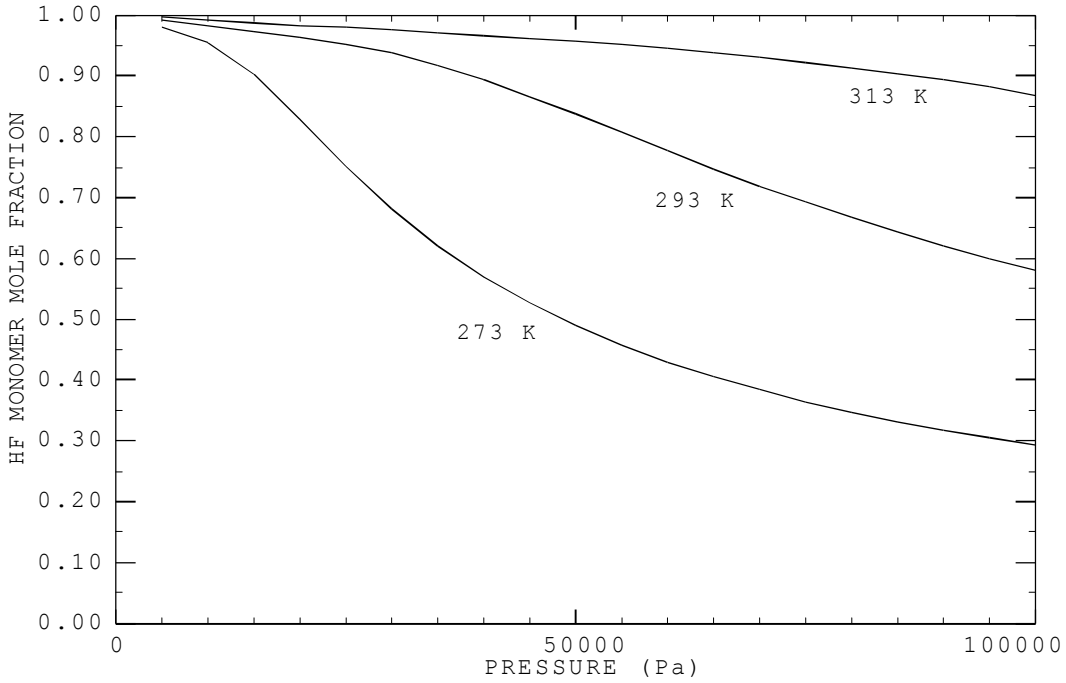


# Ground Level Dispersion

Ground level dispersion is treated using the method of Epstein et al. [36]. Epstein et al. modified the momentum equations to account for gravity compaction and sideward spreading. The ground level cross section is rectangular with a height of $2Z$ and a half-width of $b$. Entrainment is not allowed at jet-ground interface, so the perimeter of the jet is written as:

$$C = 4Z + \frac{A}{2Z} \tag{104}$$

At the transition to ground-jet dispersion, mass, concentration, and temperature are conserved. However, a discontinuity in $b$ will exist at ground contact. A new variable, $u_s$, the jet spreading velocity, is added to the governing equations. The modified governing equations are:

**Z-coordinate**

$$\frac{dZ}{ds} = \frac{Z}{A}\frac{dA}{ds} - \frac{4Z^2}{A}\left[\frac{u_e + u_s}{u}\right] \tag{105}$$

**X-coordinate**

$$\frac{dX}{ds} = 1 \qquad \theta = 0 \tag{106}$$

Figure 12: Flow and droplet trajectories for two-phase jet impinging vertically on a flat surface

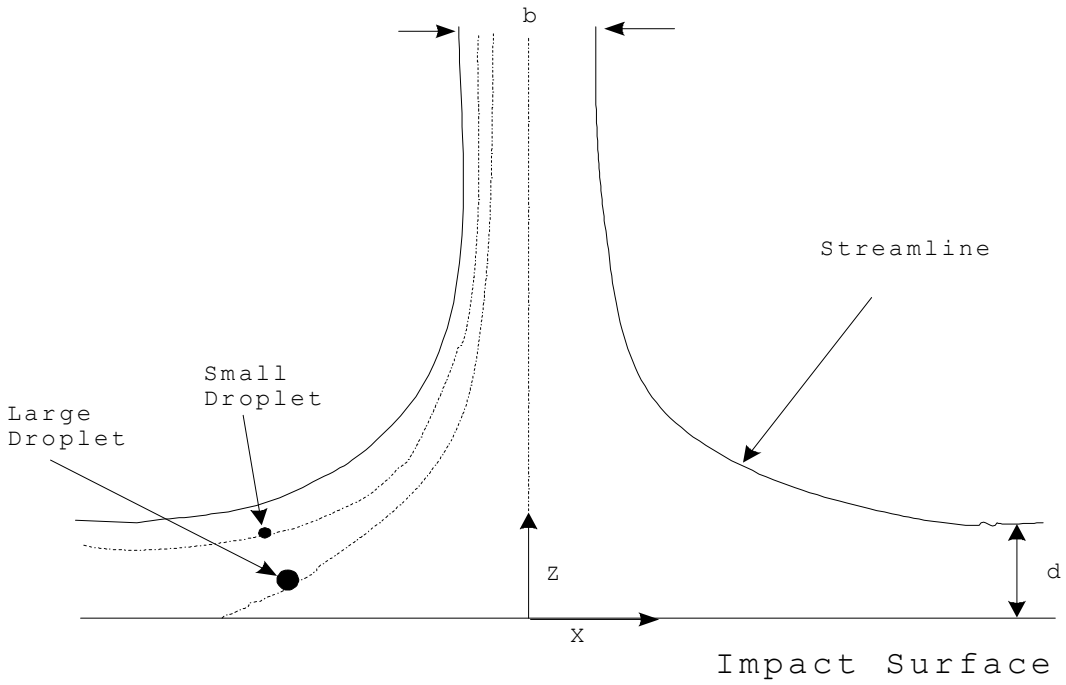


**Jet Area**

$$A = 4Zb \tag{107}$$

**Momentum for side edges**

$$\frac{d}{ds}\left[u_s\left(m_T + M_T\right)\right] = 4gZ^2\left(\rho_m - \rho_a\right) \tag{108}$$

**Momentum in axial direction**

$$\frac{d}{ds}\left[\left(m_T + M_T\right)u\right] + g\frac{d}{ds}\left[\left(\rho_m - \rho_a\right)AZ\right] = U_w\rho_a u_e\left[4Z + 2b\right] \tag{109}$$

# Jet-Obstacle Interaction

When a two-phase jet impacts a solid surface large liquid droplets are collected and rained out and smaller droplets are deflected and re-entrained in the jet. Figure 12 illustrates how the jet flow streamlines bend and flow around the impingement surface. Large droplets are not able to follow the streamlines and as a result collide with the surface while smaller droplets are carried with the flow.

The solid surface acts as an impacter and collection efficiency of liquid depends on droplet size, angle of incidence, droplet velocity, roughness and droplet thermophysical and transport

properties. Liquid collection efficiency, $\epsilon$, is defined as the ratio of the number of droplets deposited on the solid surface per unit time to the total number of droplets moving with the jet per unit time.

There are no large scale experimental data or theoretical studies that can be used to estimate liquid collection efficiency for a wide range of scenarios for pressurized liquids. However, the monographs published by Fuchs and Davis [43] can be used to estimate the liquid collection efficiency for a two-phase jet impinging normally on a flat surface. Using small scale experiments, Fuchs correlates the collection efficiency with the Stokes number:

$$N_{stk} = \frac{L}{d_j} \tag{110}$$

where $L$ is droplet stopping distance and $d_j$ is the jet diameter. $L$ is defined as the product of the droplet free stream velocity and relaxation time:

$$L = u_d \frac{m_d}{3\pi d_d \mu_{d,v}} \tag{111}$$

$\mu_{d,v}$ is the viscosity of the gas in the jet. Raj (1990) provides best-fit equations to Fuchs monograph for collection efficiency [44]:

$$\zeta = \sqrt{\frac{N_{stk}}{2}} \tag{112}$$

$$\epsilon = 0 \quad \zeta \quad 0.33 \tag{113}$$

$$\epsilon = 0.998 - 8.136\zeta + 19.254\zeta^2 - 11.408\zeta^3 \quad 0.33 < \zeta < 0.85 \tag{114}$$

$$\epsilon = 1 \quad \zeta \geq 0.85 \tag{115}$$

The Stokes number is the ratio of the droplet stop distance to a characteristic length scale of the flow, the jet diameter. $N_{stk}$ decreases as the droplet mass decreases. This implies that small droplets will quickly adopt the fluid velocity.

Jet obstacle interaction is important in the near field when air entrainment is momentum dominated. When significant momentum losses are exhibited, air entrainment occurs due to atmospheric turbulence or thermally induced turbulence for buoyant materials.

# Test Data and Validation

Validation of complex models, such as the one presented here (see Figure 7), is a difficult task. For models incorporating a large number of parameters, statistical evaluation would require a large number of experiments. Statistical evaluation based on limited experimental data can only *invalidate* a complex hazard model. Comprehensive model validation should focus on:

- correct representation of physical phenomena and underlying processes, i.e., **qualitative**,

Figure 13: Comparison of experimental values and model predictions of liquid capture fraction for several chemicals

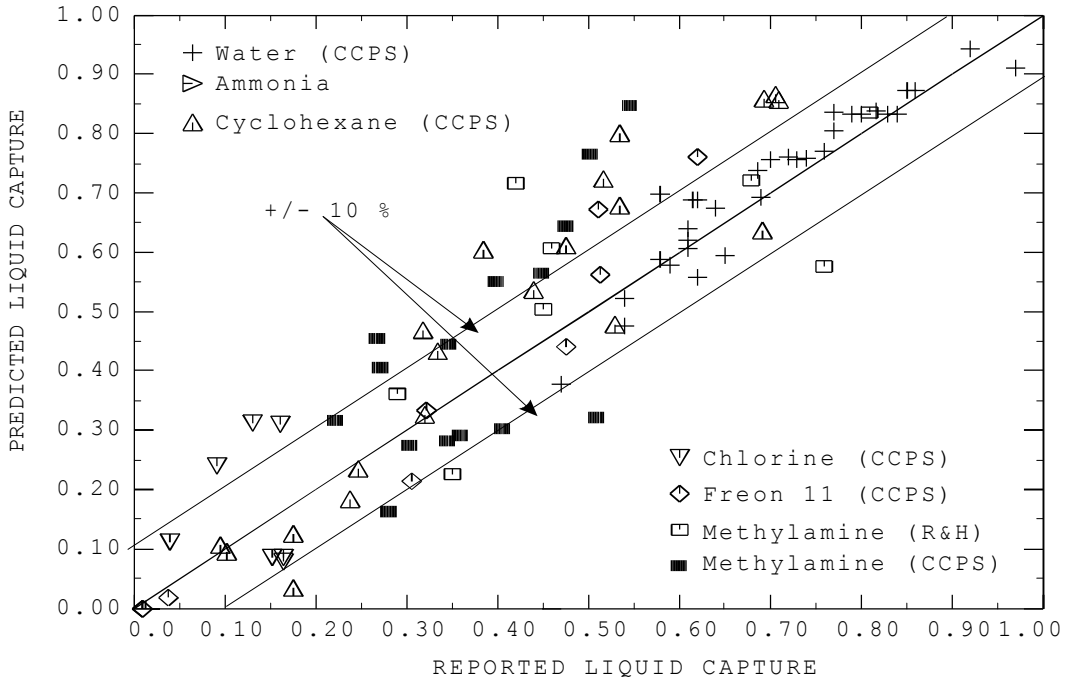


- establishing first order derivatives, i.e, **sensitivity** analysis of model predictions to input parameters, and
- comparing predictions to measured values from experiments using a given **statistical** criterion.

The model described in this chapter which includes aerosol formation, droplet evaporation and jet conservation laws was validated using large scale experimental data in both the near field and the far field. Near field validation was mainly concerned with air entrainment and its effect on temperature drop in value and location. Far field validation is mainly concerned with concentration profiles.

Typical model predictions for water, chlorine, monomethylamine, cyclohexane, and freon-11 capture data are shown in Figure 13. Excellent agreement is shown between model predictions and reported water liquid capture data. The water data shows the least amount of scatter (maximum relative error is less than 10 %) due to the low volatility of water and the high degree of superheat of most of the tests. The high degree of superheat leads to the formation of a droplet distribution with a high relative population of equal size droplets. Lower superheat, increases the drop size and leads to the formation of a droplet distribution with a wider range of droplet diameters [45]. This is graphically illustrated in Figure 14.

Both mechanical and thermal breakup regimes are accompanied by some droplet coalescence. However, it is not likely that droplet coalescence is a primary factor that needs to be included in the model. Coalescence is severely hindered by the repulsive forces caused by droplet evaporation

Figure 14: Impact of superheat on droplet size distribution

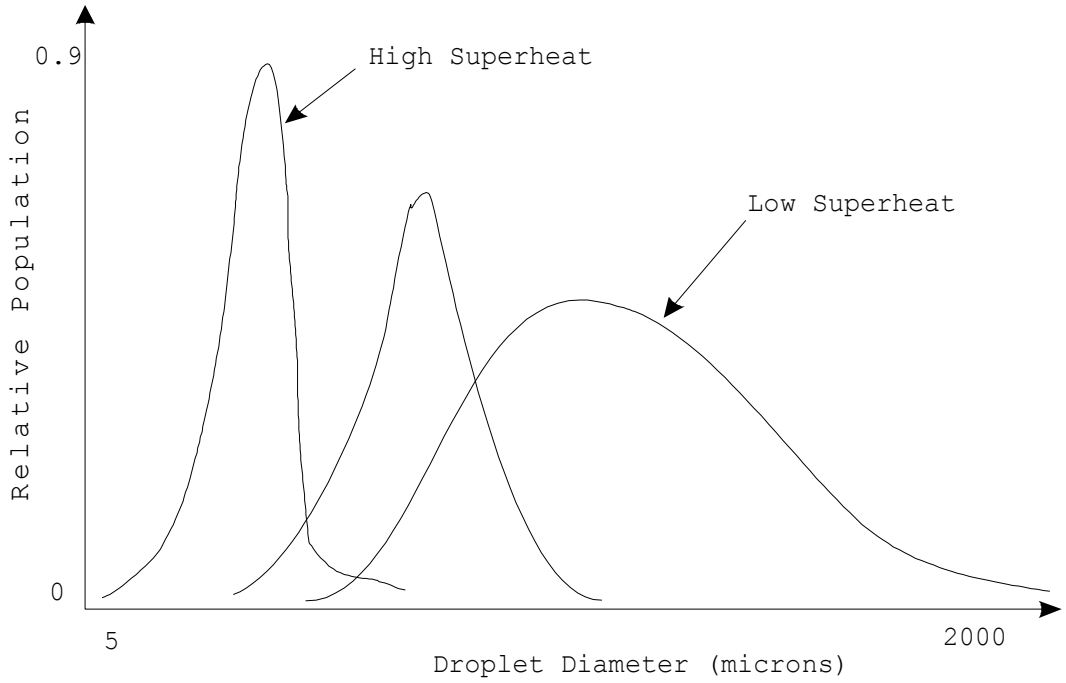


for most superheated/volatile liquids [46].

The cyclohexane, and freon-11 predictions also show a small amount of scatter due to their low volatility, i.e. droplet evaporation losses, while data for chlorine shows much more deviation. *We note here that the experimental capture data used in Figure 13 was not corrected for any evaporative losses that may have occurred in the collection pans before the contents were anlyzed.*

In addition, prediction of liquid capture is very sensitive to droplet diameter. This becomes very important at droplet diameters lower than 400 microns. This is illustrated in Figure 8. Also, Figure 15 shows a summary of experimental liquid capture data as a function of storage superheat. It is apparent from this figure that higher degrees of superheat lead to the formation of smaller droplets and as a result this leads to more evaporative losses.

Table 3 shows a range of predicted minimum temperature values for various chemicals. Figure 18 shows the concentration predictions for the Desert Tortoise ammonia experiments. Data summary can be found in reference [47].

A summary of the additized HF experiments is shown in Tables 4 and 5. The two-phase jet and aerosol formation model was used to predict the behavior of the 1992/1993 test using parameters fit based on the CCPS data. Figure 16 indicates good agreement.

Figure 15: Reported liquid capture data as a function of storage superheat

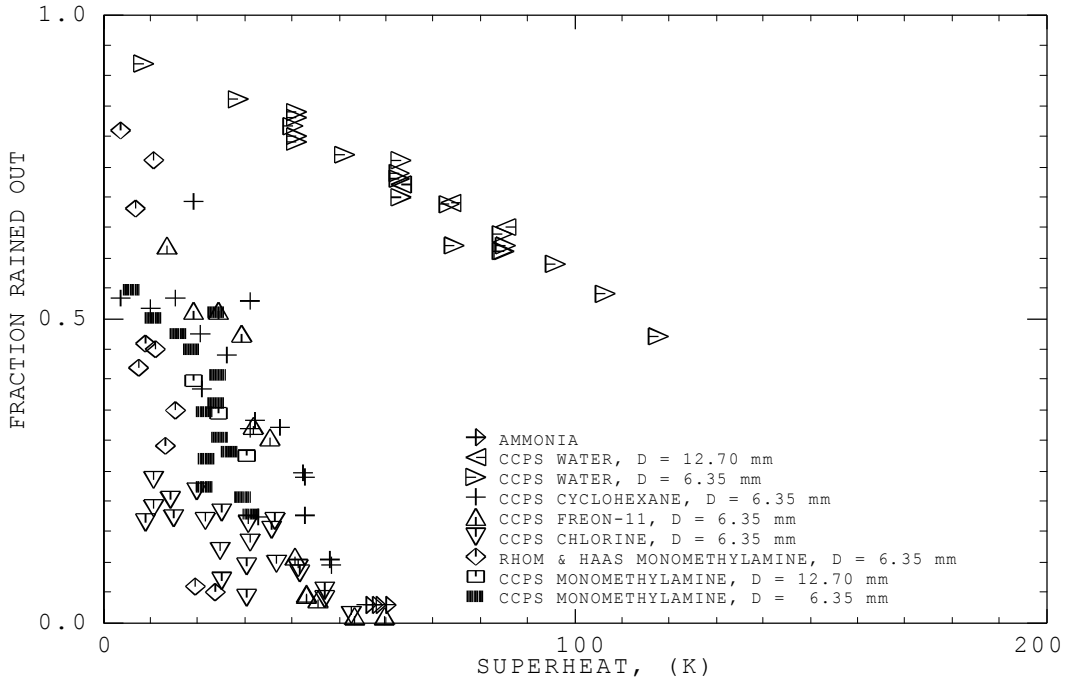


# Toxic Dispersion Hazard Reduction

In this section we consider the reduction benefits in toxic dispersion hazard footprints attributed to the additive usage. To get an approximate estimate of how much hazard footprint reduction is possible, we consider the following two simple scenarios:

- A continuous HF release at Q kg/s.
- A continuous additized HF release at 0.25 Q kg/s (75 % rainout)

We assume that farfield dispersion (i.e., to low ppm values, say 100 ppm) is well represented by a continuous Gaussian point source model. We have shown in earlier sections, that at low

Table 3: Minimum temperature predictions

| Chemical | Reported (K) | Calculated (K) |
|---|---|---|
| Chlorine | 203 - 205 | 203 - 210 |
| Freon 11 | 253 - 273 | 245 - 257 |
| Water | 298 - 315 | 290 - 310 |
| Cyclohexane | 278 - 287 | 279 - 286 |
| Methylamine | 219 - 228 | 224 - 230 |

Table 4: 1992 experimental data summary

| Run Number | T092501 | T100101 | T100102 | T100103 | T100401 | T100402 | T100403 | T100502 | T100503 | T100601 | T100602 | T100603 |
|---|---|---|---|---|---|---|---|---|---|---|---|---|
| Matrix Number | T-1 | T-2 | T-3 | T-4 | T-5 | T-6 | T-7 | T-9 | T-10 | T-11 | T-12 | T-13 |
| **Release Composition** | | | | | | | | | | | | |
| HF, mol% | 100 | 94.033 | 94.033 | 92.152 | 91.033 | 91.033 | 91.033 | 92.664 | 92.664 | 92.149 | 90.734 | 91.273 |
| Additive, mol% | 0 | 3.061 | 3.061 | 4.756 | 6.218 | 6.218 | 6.218 | 4.013 | 4.013 | 4.293 | 4.366 | 5.280 |
| Water, mol% | 0 | 2.905 | 2.905 | 3.092 | 2.749 | 2.749 | 2.749 | 3.323 | 3.323 | 3.557 | 3.734 | 3.448 |
| Isobutane, mol% | 0 | 0 | 0 | 0 | 0 | 0 | 0 | 0 | 0 | 0 | 1.2 | 0 |
| **Release Conditions** | | | | | | | | | | | | |
| $T_o$, K | 305.480 | 312.540 | 298.560 | 297.890 | 297.520 | 298.310 | 304.780 | 305.110 | 315.860 | 304.220 | 305.984 | 305.798 |
| $P_o$, kPa | 689.350 | 681.876 | 630.466 | 665.740 | 623.481 | 658.476 | 681.596 | 653.237 | 682.365 | 955.967 | 675.323 | 676.197 |
| $D_o$, mm | 6.350 | 3.175 | 12.700 | 12.700 | 19.050 | 12.700 | 12.700 | 12.700 | 12.700 | 12.700 | 12.700 | 12.700 |
| M, kg/s | 0.843 | 0.030 | 3.407 | 3.426 | 7.098 | 3.417 | 3.513 | 3.370 | 3.471 | 4.084 | 3.449 | 3.447 |
| $P_a$, kPa | 96.415 | 97.769 | 97.465 | 97.363 | 97.058 | 97.024 | 96.923 | 97.431 | 97.431 | 97.702 | 97.363 | 96.381 |
| $T_a$, K | 297.678 | 300.818 | 296.902 | 296.902 | 296.388 | 302.078 | 303.686 | 303.405 | 303.895 | 298.221 | 305.984 | 299.726 |
| C, % | 2.93 | 29.09 | 67.90 | 79.01 | 87.50 | 84.12 | 80.24 | 72.23 | 65.40 | 73.22 | 67.58 | 91.25 |
| $T_{capture}$, K | **288.258** | **293.466** | 268.147 | 269.931 | 275.139 | 275.619 | 275.831 | 273.445 | 276.299 | 274.181 | 277.143 | N/A |
| RH, % | 43.300 | 33.718 | 28.549 | 37.781 | 50.002 | 30.716 | 27.221 | 32.101 | 30.767 | 53.251 | 39.969 | 27.451 |
| $U_w$, m/s | 5.704 | 4.041 | 2.490 | 1.864 | 3.201 | 2.383 | 3.129 | 5.195 | 4.980 | 3.241 | 3.635 | 8.712 |
| **Capture Composition** | | | | | | | | | | | | |
| HF, mol % | 86.825 | 55.313 | 86.068 | 88.630 | 87.639 | 87.494 | 87.855 | 88.163 | 87.167 | 86.221 | 88.037 | 89.607 |
| Additive, mol% | 0 | 6.025 | 4.494 | 5.850 | 6.844 | 7.113 | 6.932 | 5.585 | 6.171 | 5.643 | 4.828 | 6.450 |
| Water, mol% | 13.175 | 38.662 | 9.438 | 5.521 | 5.517 | 5.394 | 5.213 | 6.251 | 6.663 | 8.137 | 7.134 | 3.943 |
| Isobutane, mol% | 0 | 0 | 0 | 0 | 0 | 0 | 0 | 0 | 0 | 0 | 0 | 0 |
| **Other** | | | | | | | | | | | | |
| Duration, s | 266.0 | 2782.0 | 55.8 | 55.4 | 48.2 | 54.8 | 46.8 | 50.0 | 44.4 | 50.2 | 36.4 | 53.8 |
| Pan Contents | Empty | Empty | Empty | Empty | Empty | Empty | Empty | Empty | Empty | Empty | Empty | Water |

| Run Number | T072001 | T072002 | T072003 | T072004 | T073001 | T073002 | T073003 | T081901 | T081902 | T081903 |
|---|---|---|---|---|---|---|---|---|---|---|
| Matrix Number | T2-1 | T2-2 | T2-3 | T2-4 | T2-5 | T2-6 | T2-7 | T2-12 | T2-13 | T2-14 |
| **Release Composition** | | | | | | | | | | |
| HF, mol% | 93.141 | 93.141 | 92.739 | 92.739 | 90.861 | 92.321 | 92.321 | 82.663 | 25.855 | 92.373 |
| Additive, mol% | 4.393 | 4.393 | 5.120 | 5.120 | 6.045 | 4.628 | 4.628 | 4.239 | 1.327 | 4.745 |
| Water, mol% | 2.467 | 2.467 | 2.141 | 2.141 | 3.094 | 3.051 | 3.051 | 2.482 | 0.772 | 2.881 |
| Surrogate, mol% | 0 | 0 | 0 | 0 | 0 | 0 | 0 | 10.616 | 72.046 | 0 |
| **Release Conditions** | | | | | | | | | | |
| $T_o$, K | 304.361 | 305.082 | 304.755 | 305.200 | 304.509 | 305.708 | 306.374 | 313.649 | 312.222 | 302.982 |
| $P_o$, kPa | 668.403 | 1612.916 | 667.824 | 351.832 | 681.925 | 676.853 | 669.935 | 640.383 | 679.709 | 753.406 |
| $D_o$, mm | 12.700 | 12.700 | 12.700 | 12.700 | 6.350 | 12.700 | 12.700 | 12.700 | 12.700 | 12.700 |
| M, kg/s | 2.913 | 4.472 | 2.931 | 2.145 | 0.714 | 2.932 | 2.933 | 1.576 | 2.736 | 2.734 |
| $P_a$, kPa | 97.160 | 97.465 | 97.194 | 97.194 | 97.194 | 97.126 | 97.126 | 97.160 | 97.024 | 96.957 |
| $T_a$, K | 305.966 | 308.751 | 309.405 | 309.306 | 306.288 | 313.373 | 312.070 | 312.100 | 312.794 | 311.484 |
| C, % | 71.64 | 64.91 | 71.55 | 76.97 | 75.06 | 71.39 | 76.90 | 61.11 | 44.79 | 68.70 |
| $T_{capture}$, K | 274.948 | 276.886 | 273.516 | 272.910 | 284.554 | 274.677 | N/A | 282.735 | 255.372 | 310.621 |
| RH, % | 54.131 | 41.416 | 38.861 | 38.419 | 51.166 | 29.433 | 31.369 | 19.383 | 19.240 | 21.610 |
| $U_w$, m/s | 4.465 | 3.411 | 4.224 | 2.472 | 2.822 | 2.463 | 4.406 | 4.313 | 2.070 | 2.529 |
| **Capture Composition** | | | | | | | | | | |
| HF, mol % | 67.851 | 78.690 | 86.319 | 88.206 | 76.127 | 84.882 | 89.167 | 75.168 | 52.027 | 80.587 |
| Additive, mol% | 5.991 | 6.556 | 6.306 | 6.338 | 7.838 | 6.694 | 6.851 | 7.997 | 6.491 | 6.400 |
| Water, mol% | 26.158 | 14.754 | 7.375 | 5.456 | 16.035 | 8.424 | 3.982 | 16.836 | 41.481 | 13.013 |
| Surrogate, mol% | 0 | 0 | 0 | 0 | 0 | 0 | 0 | 0 | 0 | 0 |
| **Other** | | | | | | | | | | |
| Duration, s | 71.0 | 75.4 | 176.5 | 87.0 | 242.5 | 60.4 | 66.8 | 162.0 | 86.2 | 87.8 |
| Pan Contents | Empty | Empty | Empty | Empty | Empty | Empty | Water | Empty | Empty | Empty |

Table 5: 1993 experimental data summary

Figure 16: Comparison of experimental values and model predictions of liquid capture fraction for HF and additized HF. 1992/1993 data

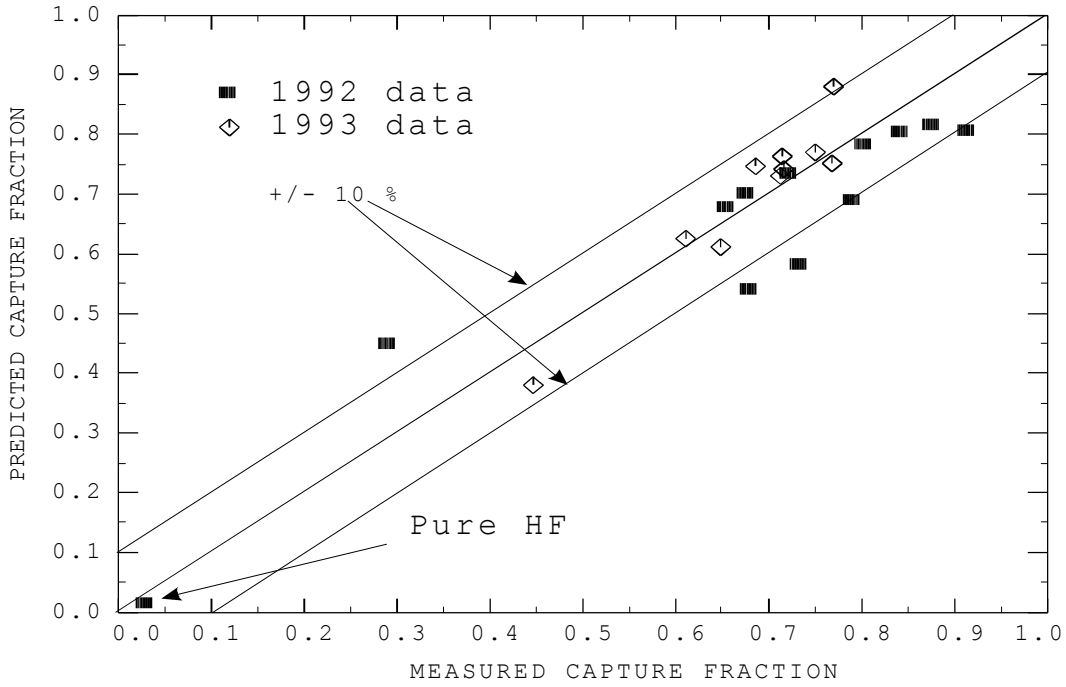


concentrations, HF exists as monomer in the vapor cloud due to its low partial pressure. Under F atomoshperic stability and a roughness length of 0.1 m, the centerline concentration at any given downwind distance can be estimated using the following equation:

$$C(x) = \frac{Q}{2\sigma_y \sigma_z u_x \pi} \tag{116}$$

where $C$ is the concentration in $\mathrm{kg/m^3}$, $u_x$ is the wind speed (assumed value of 2 m/s), and $\sigma_y$ and $\sigma_z$ are the Gaussian standard deviations which can be approximated using the following relations:

$$\sigma_y = 0.065x^{0.902} \tag{117}$$

$$\sigma_z = 0.120x^{0.67} \tag{118}$$

These equations can be reduced and solved analytically for downwind distance at a specified limiting concentration value. At the same limiting concentration, the downwind distance ratio of additized to non-additized HF release is given by:

$$\frac{x_{HF,additized}}{x_{HF}} = \left[\frac{0.25Q}{Q}\right]^{\frac{1}{1.572}} = 0.40 \tag{119}$$

This indicates that a 75 % reduction in emission rate will result in a 60 % reduction in downwind distance.

Table 6: Additized hydrogen fluoride hazard reduction benefits

| | No Additive | Additized | Ratio |
|---|---|---|---|
| Ambient temperature (K) | 298 | 298 | |
| Ambient pressure (kPa) | 100 | 100 | |
| Relative humidity (percent) | 50 | 50 | |
| Surface roughness length (m) | 0.1 | 0.1 | |
| Stability Class | F | F | |
| Averaging time (min) | 10 | 10 | |
| 3 m wind speed (m/s) | 2 | 2 | |
| | | | |
| Release height (m) | 2 | 2 | |
| Source temperature (K) | 305 | 305 | |
| Source pressure (kPa) | 685 | 685 | |
| Orifice diameter (mm) | 50.8 | 50.8 | |
| Release rate (kg/s) | 55.5 | 55.5 | |
| Additive fraction (mol percent) | 0 | 6.3 | |
| | | | |
| Maximum droplet diameter (microns) | 205 | 1800 | 0.113 |
| Downwind Distance (m) | 6900 | 4100 | 0.59 |
| Hazard area $(\mathrm{m}^2)$ | $6.32 \times 10^6$ | $1.07 \times 10^6$ | 0.17 |

We used a simple Gaussian analysis to illustrate the benefits of using the additive on toxic hazard downwind distance reduction. This approach is limited and does not accurately represent how the hazard footprint is impacted due the presence of aerosols.

We will use the detailed dispersion model developed in this paper to illustrate the benefits of using the additive on hazard footprint reduction. The presence of the aerosols will lead to a heavier cloud and thus a larger footprint. If the aerosols rainout, the footprint will be smaller.

We consider a hypothetical release of hydrogen fluoride from a 50.8 mm orifice (2 inch) at 2 m elevation. Details pertaining to this scenario are shown in Table 6. Figure 17 illustrates the impact of the additive on toxic hazard reduction. The hazard area is reduced by 83 %. A significant reduction in hazard area will lead to a significant reduction is risk.

# 1 Conclusion

This additive technology represents a viable method for reducing the consequences of two-phase hydrogen fluoride releases. The sensitivity of liquid rainout and subsequent pool formation to storage conditions can be assessed using the model developed in this paper for the estimation of droplet size, droplet evaporation and two-phase jet dispersion.

Figure 17: Additized hydrogen fluoride hazard reduction benefits. Concentration and footprint profiles to 100 ppm.

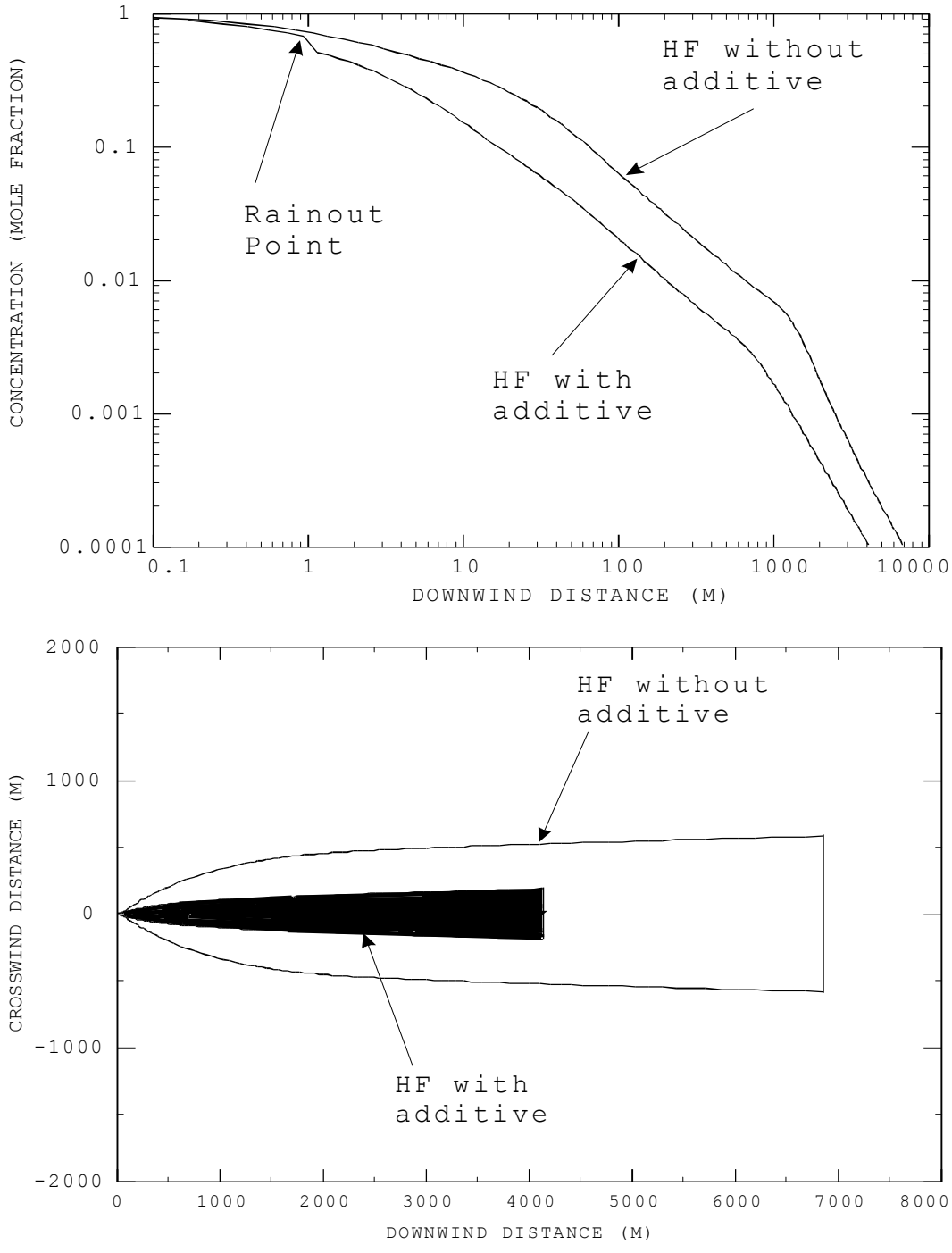

Figure 18: Far field model predictions

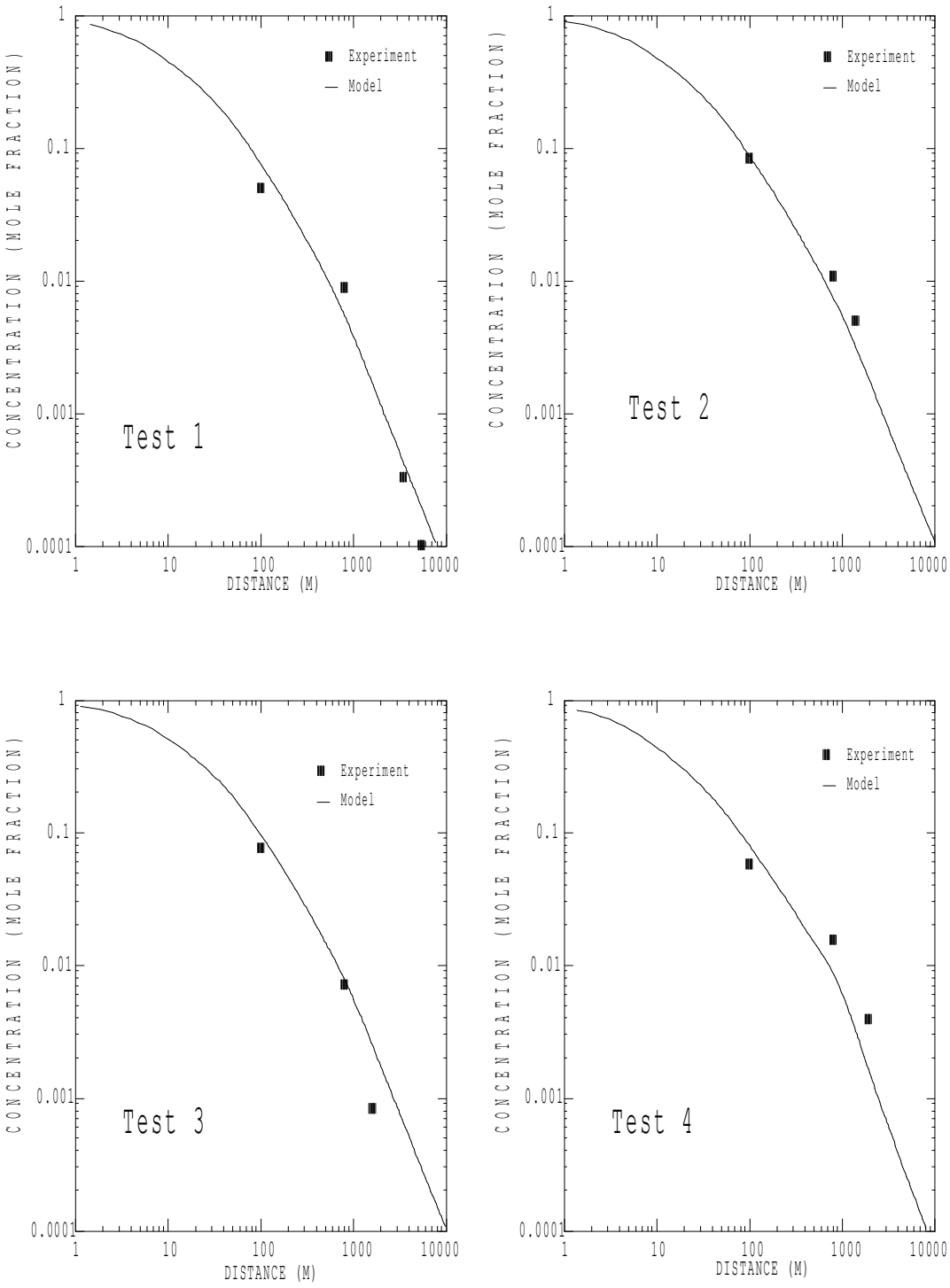

**List of Symbols**

| | |
|---|---|
| A | Area, $(m^2)$ |
| $A_E$ | Available energy, $(J/kg)$ |
| b | Homogeneous radius, $(m)$ |
| D, d | Diameter, $(m)$; Diffusivity, $m^2/s$ |
| C | Concentration, (volume percent); Percent liquid capture |
| $C_D$ | Drag coefficient |
| $C_p$ | Heat capacity at constant pressure, $(J/kmol/K)$ |
| F | Flash fraction |
| g | Acceleration due to gravity, $(9.8 m/s^2)$ |
| G | Gibbs free energy |
| h | Heat transfer coefficient, $(J/s/m^2/K)$ |
| H | Enthalpy, $(J/kmol)$ |
| k | Thermal conductivity, $(J/m/s/K)$ |
| K | Equilibrium constant; mass transfer coefficient |
| L | Monin-Obukov length scale, $(m)$ |
| m | Liquid mass, $(kg)$ |
| M | Mass; vapor mass, $(kg)$ |
| Mw | Molecular weight, $(kmol/kg)$ |
| n | Liquid number of moles, $(kmol)$ |
| N | Number of moles; vapor number of moles, $(kmol)$ |
| $N_{Pr}$ | Prandtl number |
| $N_{We}$ | Weber number |
| $N_{Ri}$ | Richardson number |
| $N_{Re}$ | Reynolds number |
| $N_{Nu}$ | Nusselt number |
| $N_{Sc}$ | Schmidt number |
| $N_{Sh}$ | Sherwood number |
| P | Pressure, $(Pa)$ |
| q | Heat flux, $(J/m^2/s)$ |
| Q | Heat, $(J)$ |
| $R_g$ | Universal gas constant, 8314 $(J/kmol/K)$ |
| RH | Percent relative humidity |
| R, r | Radius, $(m)$ |
| s | Curvilinear distance |
| t | Time, $(s)$ |
| T | Temperature, $(K)$ |
| u | Velocity, $(m/s)$ |
| U | Internal energy, $(J/kmol)$ |
| Uw | Wind speed, $(m/s)$ |
| V | Volume; vapor volume, $(m^3)$ |
| v | Liquid volume, $(m^3)$ |
| x | Horizontal distance; downwind distance, $(m)$ |
| y | Crosswind distance, $(m)$ |
| z | Vertical distance; height; elevation; depth, $(m)$ |

**Subscripts**

| | |
|---|---|
| a | Air |
| c | Critical; centerline |
| C | Chemical |
| d | Droplet |
| e | Evaporation; entrainment |
| f | Friction; final |
| g | Gas |
| in | Input |
| j | Jet |
| l | Liquid |
| m | Mixture |
| 0 | Initial; reference |
| out | Output |
| r | Reduced |
| s | Spill surface; surroundings |
| sat | Saturated |
| sh | Superheated |
| T | Total |
| t | Terminal |
| v | Vapor |
| vl | Vapor-Liquid interface |
| w | Water |
| $\underline{x}$ | Molar |

**Superscripts**

| | |
|---|---|
| $\dot{x}$ | Rate, x units/s |
| $\overline{x}$ | Partial molar |
| $\hat{x}$ | Non-ideal |

**Greek Symbols**

| | |
|---|---|
| $\rho$ | Density, $(kg/m^3)$ |
| $\nu$ | Kinematic viscosity, $(m^2/s)$ |
| $\mu$ | Viscosity, $(kg/m/s)$ |
| $\sigma$ | Surface tension, $(kg/s^2)$ |
| $\alpha$ | Thermal diffusivity, $(m^2/s)$; void fraction |
| $\lambda$ | Latent heat of vaporization, (J) |
| $\pi$ | 3.141592654 |
| $\gamma$ | Heat capacity ratio, $(C_p/C_v)$ |
| $\Phi$ | Fugacity coefficient |
| $\theta$ | Angle with respect to horizontal |
| $\tau$ | Stress or applied force per unit area, Pa |

# References

[1] D. N. Blewitt, J. F. Yohn, R. P. Koopman, and T. C. Brown. Conduct of anhydrous hydrofluoric acid spill experiments, 1987.

[2] R. Brown and J. L. York. Sprays formed by flashing liquid jets. *AIChE Journal*, 8(2):149–153, 1962.

[3] D. M. Bushnell and P. B. Gooderum. Atomization of superheated water jets at low ambient pressures. *Journal of Spacecraft*, 5(2):231–231, 1968.

[4] J. O. Hinze. Fundamentals of the hydrodynamic mechanism of splitting in dispersion processes. *AIChE Journal*, 1(4):289–295, 1955.

[5] A. Brodkey. *The Phenomenon of Fluids Motions*. Addison-Wesley, 1967.

[6] V. Iannello, G. B. Wallis, and P. H. Rothe. Liquid release. Prepared for the AIChE Center for Chemical Process Safety TM-1274, Creare Inc., 1988.

[7] H. K. Forester and N. Zuber. Growth of a vapor bubble in a superheated liquid. *Journal of Applied Physics*, 25(4):474–478, 1954.

[8] M. S. Plasset and S. A. Zwick. The growth of vapor bubbles in superheated liquids. *Journal of Applied Physics*, 25(4):493–500, 1954.

[9] J. E. Shepherd and B. Sturtevant. Rapid evaporation at the superheat limit. *Journal of Fluid Mechanics*, 121:379–402, 1982.

[10] H. Kwak and S. Lee. Homogeneous bubble nucleation predicted by a molecular interaction model. *Transaction of the ASME*, 113:714–721, 1991.

[11] J. H. Lienhard and J. B. Day. The breakup of superheated liquid jets. *J. Basic Eng., Trans. AIME*, page 515, 1970.

[12] G. A. Melhem and R. Saini. A model for the dispersion of two-phase multicomponent jets, 1992.

[13] R. J. Lantzy, R. D. Myers, D. B. Pfenning, and S. B. Millsap. Atmospheric release tests of monomethylamine. *Journal of Loss Prevention*, 3:77, 1990.

[14] Energy Analysts Inc. Release characteristics of superheated water and CFC-11 liquids. Experimental Data 90-05-540, The Center for Chemical Process Safety, 1990.

[15] Quest Consultants Inc. Release behavior of superheated chlorine, methylamine, and cyclohexane. Experimental Data 91-05-6012, The Center for Chemical Process Safety, 1991.

[16] G. A. Olah. Environmentally safe catalytic alkylation using liquid onium poly(hydrogen fluorides, US patent number 5,073,674.

[17] D. N. Blewitt, J. F. Yohn, and D. L. Ermak. An evaluation of slab and degadis heavy gas dispersion model using the hf spill test data, 1987.

[18] S. T. Chan, H. C. Rodean, and D. N. Blewitt. Fem3 modeling of ammonia and hydrofluoric acid dispersion, 1987.

[19] K. W. Schatz and R. P. Koopman. Effectiveness of water spray mitigation systems for accidental releases of hydrogen fluoride. summary report and volumes I-X, 1989.

[20] K. W. Schatz, G. R. Jersey, M. K. Chalam, and D. W. Johnson. Apparatus for field testing of hf releases, 1993.

[21] A. Papadourakis, H. S. Caram, and C. L. Barner. Upper and lower bounds of droplet evaporation in two-phase jets. In *Health and Safety Symposium, Spring National Meeting*. American Institute of Chemical Engineers, 1990.

[22] T. Vesala and J. Kukkonen. A model for evaporation of freely falling droplets. Publications on air quality 6, Finnish meteorological institute, 1989.

[23] J. Kukkonen and M. Kumala. Estimating the aerosol behavior of a turbulent two-phase jet. *Journal of Aerosol Science*, 18(6):643–645, 1987.

[24] J. Kukkonen and T. Vesala. The importance of aerosol phenomena in estimating the atmospheric dispersion of hazardous substances. *Finnish association for aerosol research report series*, (5):106–110, 1988.

[25] J. Kukkonen, T. Vesala, and M. Kumala. The evaporation of airborne droplets in a turbulent two-phase jet. *Journal of aerosol science*, 19(7):871–874, 1988.

[26] J. L. Woodward and A. Papadourakis. Modeling of droplet entrainment and evaporation in a dispersing jet. In *International conference and workshop on modeling and mitigating the consequences of accidental releases of hazardous materials*, pages 147–167. CCPS, AIChE, 1991.

[27] P. E. Wagner. Aerosol growth by condensation. In *Aerosol Microphysics II*, pages 129–178. Springer-Verlag, 1982.

[28] G. Ooms. A new method for the calculation of the plume path of gases emitted by a stack. *Atmospheric Environment*, 6:899, 1972.

[29] G. Ooms, A. P. Mahieu, and F. Zelis. The plume path of vent gases heavier than air. In *First International Symposium: Loss Prevention and Safety Promotion in The Process Industries.*, 1974.

[30] G. Abraham. The flow of round buoyant jets issuing vertically into an ambient fluid flowing in a horizontal direction. In *5th International Water Pollution Research Conference*, page 15/1, 1970.

[31] D. P. Hoult, J. A. Fay, and L. J. Forney. A theory of plume rise compared with field observations. *Journal of Air Pollution Control Association*, 19:585, 1969.

[32] F. P. Ricou and D. B. Spalding. Measurments of entrainment by axisymmetric turbulent jets. *Journal of Fluid Mechanics*, 11:21, 1961.

[33] G. A. Briggs. Chimney plumes in neutral and stable surroundings. *Atmospheric Environment*, 6:507–510, 1972.

[34] G. A. Briggs. Plume rise. AEC Critical Review Series TID-25075, National Information Service, U.S. Department of Commerce, 1969.

[35] J. C. Kaimal, J. C. Wyngaard, D. A. Haugen, O. R. Cote, and Y. Izumi. Turbulence structure in the convective boundary layer. *J. Atmos. Sci.*, 33, 1976.

[36] M. Epstein, H. K. Fauske, and G. M. Hauser. A model of the dilution of a forced two-phase chemical plume in a horizontal wind. In *1990 Spring National Meeting*, pages 1–40. AIChE, 1990.

[37] R. Saini. Computation of complex equilibria using successive quadratic programming. Master's thesis, Northeastern University, 1988.

[38] G. A. Melhem, R. Saini, and B. M. Goodwin. A modified Peng-Robinson equation of state. *Fluid Phase Equilibria*, 47:189–237, 1989.

[39] W. V. Wilding, L. C. Wilson, L. V. Jasperson, H. L. Wilson, and G. M. Wilson. Vapor PVT and vapor pressure data of hydrogen fluoride. In *Spring National Meeting*. AIChE, 1993.

[40] C. H. Twu, J. E. Coon, and J. R. Cunningham. An equation of state for hydrogen fluoride. *Fluid Phase Equilibrium*, 86:47–62, 1993.

[41] P. C. Gillespie, J. R. Cunningham, and G. M. Wilson. Vapor-liquid equilibrium measurements for the hydrogen fluoride/hydrogen chloride system. In *AIChE Symposium Series, 81 (244)*, pages 41–48. AIChE, 1985.

[42] J. H. Seinfeld. *Atmospheric chemistry and physics of air pollution*. Wiley, 1986.

[43] N. A. Fuchs and C. N. Davis (Editors). *The Mechanics of Aerosols*. Pergamon Press, 1964.

[44] P. K. Raj. Considerations of liquid aerosol formation and entrainment in a two-phase heavy gas jet dispersion. In *Health and Safety Symposium*, pages 1–21. AIChE, 1990.

[45] M. Razzaghi. Droplet size estimation of two-phase flashing jets. *Nuclear Engineering and Design*, 114:115–124, 1989.

[46] V. A. Fedoseev. Dispersion of a stream of superheated liquid. *Colloid Journal*, 20:463, 1958.

[47] S. R. Hanna, D. G. Strimaitis, and J. C. Chang. Evaluation of 14 hazardous gas models with ammonia and hydrogen fluoride field data. Technical paper, Sigma Research Corporation, 1991.